Available online at www.CivileJournal.org

Civil Engineering Journal

(E-ISSN: 2476-3055; ISSN: 2676-6957)

Vol. 10, No. 09, September, 2024

Effectiveness of Different Configurations of Ferrocement Retrofitting for Seismic Protection of Confined Masonry: A Numerical Study

Ahmad B. Habieb [1*], Muhammad R. Hidayat [1], Wahyuniarsih Sutrisno [1], Nurmurat Kandymov [2], Gabriele Milani [3]

[1] *Department of Civil Engineering, Sepuluh Nopember Institute of Technology, Surabaya, Indonesia.*

[2] *Department of Civil Engineering, Paragon International University, Phnom Penh 12510, Cambodia.*

[3] *Department of Architecture, Built Environment and Construction Engineering (ABC), Politecnico di Milano, 20133 Milan, Italy.*

Received 08 May 2024; Revised 17 August 2024; Accepted 23 August 2024; Published 01 September 2024

Abstract

A ferrocement layer, which consists of a wire mesh and cement mortar, is a popular retrofitting method for existing structural elements, particularly wall or slab panels. This paper presents a study on the effectiveness of different configurations of ferrocement for seismic retrofitting of confined masonry through finite element analysis. The masonry panel was modeled using expanded brick-unit elements, where the element was expanded in size by as much as half of the mortar thickness, and an interacting zero-thickness interface was applied to mimic the elastic-plastic and damage behavior during tension, shear, and compression. The concrete damage plasticity (CDP) model was used to model the confining reinforced concrete frame and overlay mortar in the ferrocement layer, and the reinforcing bars and wire mesh were modeled using elastic-plastic behavior. In the present numerical study, nine models were subjected to cyclic and pushover shear test simulations, considering the effects of the number of ferrocement layers and the wire mesh orientation. The volumetric ratio of the wire mesh to the masonry (ρ_{wm}) ranged from 0.48% to 1.92%, whereas the ratio of the mortar overlay to the masonry (ρ_{mo}) varies from 10.42% to 41.66%. Based on the increase in the lateral strength, the model with the largest volume of the ferrocement layer exhibited the largest increase in strength. However, the most cost-effective retrofitting configuration was presented by model DS-1-45, in which a single layer of ferrocement was applied on both sides of the wall using 45° of wire mesh orientation. The DS-1-45 model provided a lateral strength increase of more than 6 times compared to the original unreinforced model.

Keywords: Ferrocement; Seismic Retrofitting; Earthquake-Risk Mitigation; Strengthening; Masonry; Finite Element Analysis; Expanded Unit Model; Concrete Damage Plasticity.

1. Introduction

In the event of earthquakes, residential masonry buildings are very vulnerable to destruction [1–3]. Residential buildings, particularly in developing regions, are generally built using low-cost materials by unskilled local workers. For instance, in Indonesia, the most commonly used structural systems for low-rise residential buildings in rural areas are unreinforced masonry (UM) and confined masonry (CM) [4, 5]. These structures are very vulnerable to lateral forces because they rely only on the shear or flexural strength of the masonry walls, which are provided almost entirely by the mortar interface [6-11]. In the case of CM structures, the confining reinforced concrete frame may improve the masonry integrity or increase its ductility. However, insufficient frame dimensions or a lack of detailing procedures during construction can lead to ineffective reinforcement.

* Corresponding author: ahmad.basshofi@its.ac.id

http://dx.doi.org/10.28991/CEJ-2024-010-09-02

To this day, UM or CM structures are still popular in developing regions, even in areas with high seismicity, because of their low construction costs. In addition, control by local authorities regarding the importance of earthquake resistance in low-rise residential buildings is lacking, unlike supervision in large buildings. This has encouraged researchers and engineers to develop low-cost seismic retrofitting methods suitable for substandard low-rise residential buildings.

Several materials have been introduced as retrofitting elements for masonry, such as ferrocement (i.e., wire mesh and mortar overlay), engineered cementitious composites (ECC), fiber-reinforced polymers (FRP), polypropylene (PP) bands, and bamboo strips. In general, these reinforcing elements are applied to resist the tensile force or flexural action that occurs during earthquakes.

Sandoval et al. [12] investigated the performance of strengthened masonry panels using a welded wire mesh. Through a series of monotonic and cyclic diagonal shear-compression tests, the strength and stiffness were found to increase by 2.3 and 3.2 times, respectively, compared to the original masonry panel. The study concluded that using a 0.33% steel content in the masonry panel presented the most effective strengthening effect. In a study by Shermi et al. [13], the in-plane performance of an unreinforced masonry panel strengthened with a welded wire mesh and mortar was investigated through experimental tests. A significant increase in the shear strength was observed in the retrofitted models. Such composite systems consisting of a mortar matrix and a steel wire mesh are often called ferrocement. It may generate composite action against external loads: the wire mesh is useful to resist tensile action, and the cement mortar is useful to resist compressive action when subjected to an earthquake. Banerjee et al. [14] experimentally and numerically studied a brick masonry panel retrofitted using a steel wire mesh. The results indicate that the load-carrying capacity, shear strength, and deformability of the retrofitted masonry panel were enhanced.

Warjri et al. [15] experimentally studied masonry panels embedded with a steel-welded wire mesh and mortar overlay. The study considered various volumes and patterns of the wire mesh. It was found that the model fully covered with wire mesh presented an almost two-fold increase in the lateral strength. A numerical study by Debnath et al. [16] investigated the performance of retrofitted masonry walls using wire meshes, considering different types of brick bonds and the aspect ratio of the walls. It was found that the type of brick bond slightly affected the strength increase after the wire mesh reinforcement. De Santis et al. [17] studied the use of steel reinforcement and mortar grouting on U-shaped masonry walls. Based on the shaking table test, the retrofitted specimen exhibited a lateral strength 5.1 times greater than the original structure.

Xin et al. [18] experimentally studied the restoration of damaged masonry walls using grout-injected ferrocement overlay. Based on the results of the cyclic shear tests, the ultimate resistance and residual strength were increased by approximately 6% and 13%, respectively. In addition, the ultimate and residual deformations dramatically increased by approximately 110% and 60%, respectively. The failure mode changed from diagonal shear to flexural dominant, indicating an improvement in the shear capacity of the restored masonry walls. Saingam et al. [19] investigated the use of ferrocement overlays to enhance the flexural capacity of cement-clay interlocking (CCI) brick walls by considering the effects of mesh size and anchor configuration. The strengthened panels with one-sided and two-sided ferrocement overlays presented remarkable increases in the flexural peak capacity by 28% and 64%, respectively.

In another case, ECC mortar was used as the retrofitting material in the experimental study by Deng and Yang [20]. The application of ECC coating on one side and both sides of the masonry wall resulted in maximum increases in the lateral in-plane strength by 116% and 247%, respectively. Umair et al. [21] investigated the effect of FRP and PP band composites on the reinforcement of UM structures undergoing in-plane compression and flexural out-of-plane loads. It was found that the retrofitting approach did not only significantly increase the peak lateral strength and ductility of the masonry structures.

In an experimental study by Jang et al. [22], glass-fiber-reinforced polyurea (GFRPU) was used as a reinforcing material to enhance the out-of-plane capacity of unreinforced masonry panels. It was demonstrated that one-sided complete reinforcement can significantly improve the out-of-plane strength and ductility with such a low-cost retrofitting method. A comprehensive study on the efficiency of several retrofitting materials for masonry structures was performed by Courasie et al. [23], where grid meshes made of plastic, nylon, polypropylene, and fabric were used as reinforcement for masonry specimens that were subjected to quasi-static lateral loading. Habieb et al. [5] conducted pushover shear tests on masonry specimens retrofitted with bamboo strips on both sides. It was found that the use of bamboo strips with a bamboo-to-masonry volume ratio of 2.88% resulted in a 1.6-fold increase in peak lateral strength and a 15-fold increase in ultimate lateral deformation.

On the other hand, the use of seismic isolation and energy dissipation devices has also been presented in the study of the protection of UM buildings. In the literature of Habieb et al. [24], a hybrid isolation system using fiber-reinforced elastomeric isolators (FREIs) and shape memory alloy wires (SMA) was proposed for the protection of a historical masonry church. Based on the numerical analysis, the damage to the masonry could be significantly reduced under the considered earthquakes thanks to the reduction in the seismic force demand provided by the isolation system. Boni and Royer-Carfagni [25] proposed transparent hybrid glass-steel bracing to improve the seismic capacity of historic masonry

buildings. Based on the analytical study, the correct design and positioning of the proposed devices can improve the lateral capacity of historical masonry buildings without disrupting their architectural appearance.

Among several retrofitting methods mentioned above, the ferrocement material (i.e., wire mesh and mortar overlay) appears to show superior strengthening effects in masonry structures. The wide availability and easy application of wire mesh materials make them one of the most suitable options for retrofitting existing buildings. In addition, its high strength is guaranteed by industrial fabrication [26, 27]. However, the effects of the ferrocement volume and configuration need to be further investigated, considering a wider range of mortar and wiremesh volumes. Therefore, in the present study, the effects of the volume and orientation of the ferrocement layer were investigated through numerical analyses to provide a reference for determining the optimum volume of retrofitting materials for specified performance targets. Numerical analyses were performed based on the simplified micromodel of CM panels subjected to lateral cyclic shear loads. The peak strength, deformability, and energy dissipation of the original and retrofitted models were evaluated.

2. Research Methods

As shown in the flowchart in Figure 1, the study started with a literature study and numerical modeling of the CM panel and ferrocement layer tested in an experimental study [20, 28]. The material and interaction properties were estimated through available code or literature and then validated with the test results reported in the experimental study. When all the model parameters were set, a series of shear test-FE simulations was performed to investigate the effect of different ferrocement configurations.

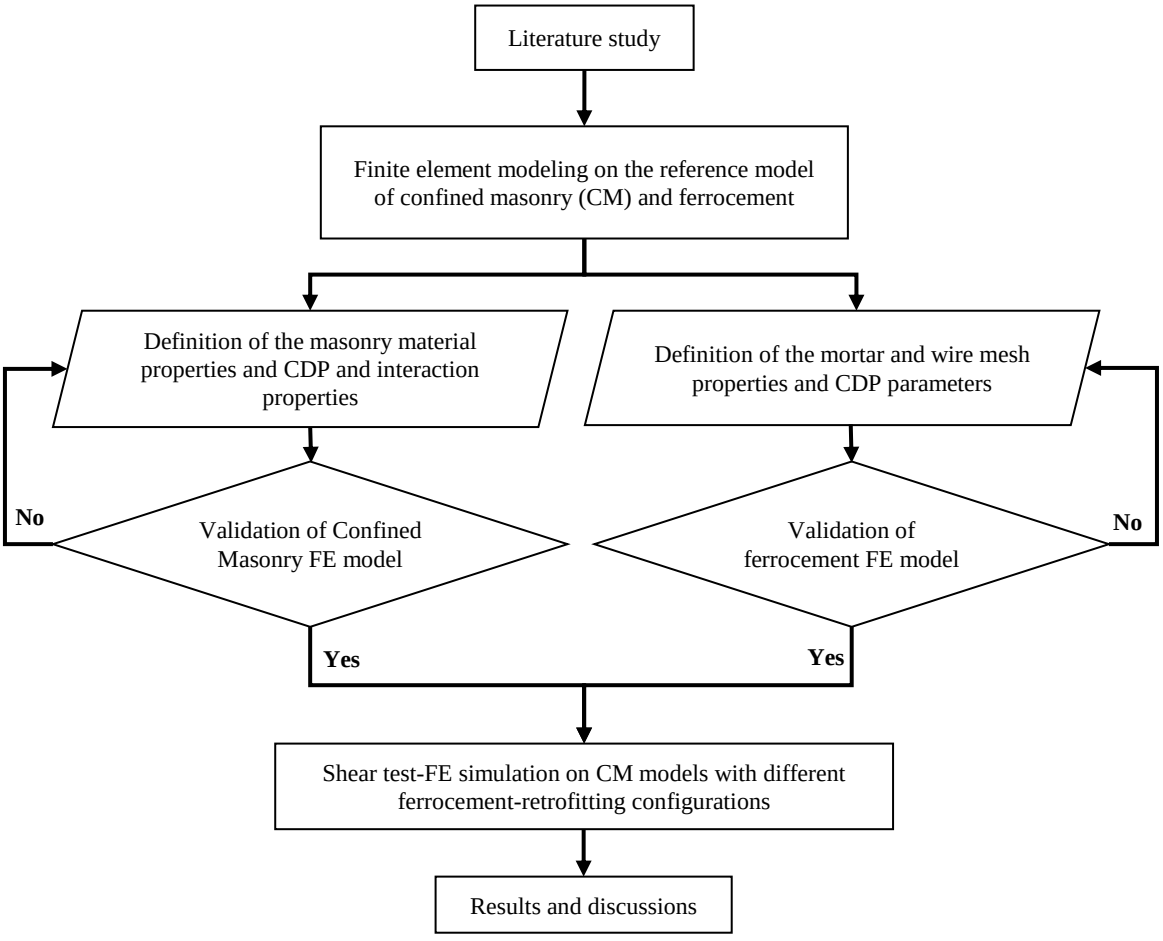

Figure 1. Research flowchart

2.1. Model Reference for Confined Masonry and Ferrocement

The model of CM panel experimentally tested by Deng & Yang [20] was used as a reference model in this study, as shown in Figures 2-a and 2-b, where a flemish brick bond was used (see Figure 2-c). The dimensions of the CM panel were 2300 × 1370 × 240 mm, resulting in a height to length ratio of 0.6. The masonry panel was confined by reinforced concrete (RC) tie beams and columns with dimensions of 240 × 120 mm. An anchorage system was applied at the base of the masonry panel to prevent premature rocking failure or sliding on the panel.

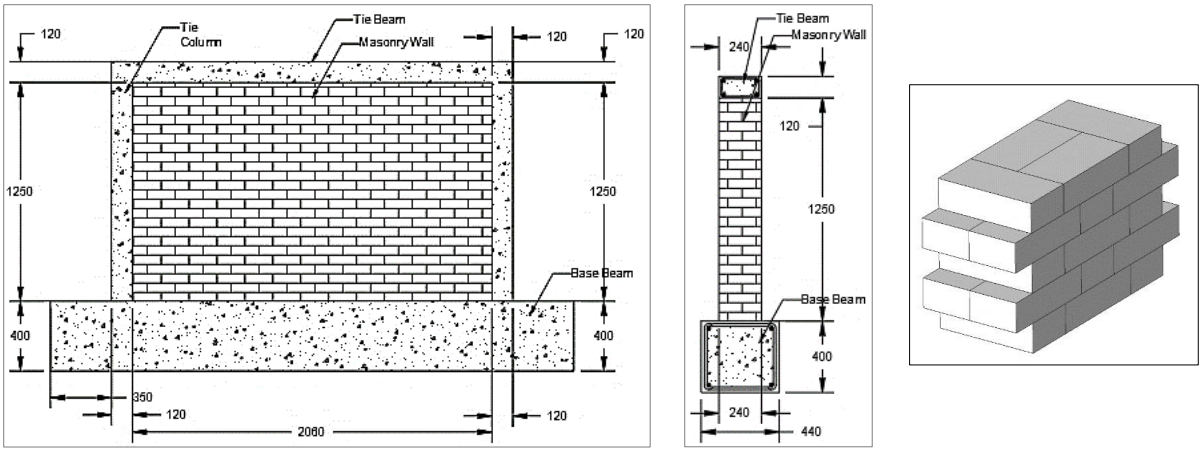

(a) (b) (c)

Figure 2. (a), (b) Dimensions of the CM specimen [20], and (c) Flemish brick bond (unit in mm)

The RC beams and columns were built using four longitudinal bars with a diameter of 12 mm and yield and ultimate strengths of 372 and 405 MPa, respectively. The transversal reinforcement has a diameter of 6.5 mm and yield and ultimate strength of 338 and 405 MPa, respectively. The transversal reinforcements were distributed at 200-mm distances along the beams and columns. The masonry panel was constructed using cement-lime mortar with an average compressive strength of 1.89 MPa and a brick unit with dimensions of 240 × 115 × 53 mm. The experimental test results obtained from the CM panel described above were used in this study to validate the numerical model without retrofitting.

To validate the numerical model of the reinforced ferrocement layer (i.e., mortar with mesh reinforcement), the experimental results reported in the literature by Miah et al. [28] were referenced. A ferrocement layer containing a 25-mm-thick mortar and a wire mesh was used to strengthen the reinforced concrete (RC) beam, as shown in Figure 3. The mortar in the ferrocement layer was made with a sand-to-cement ratio of 2:1 and a water-to-cement ratio of 0.45 and a compressive strength f_m of 40 MPa. The fine aggregates had dimensions less than 4.75 mm, a fineness modulus of 3.1, and a specific gravity of 2.56. Meanwhile, the coarse aggregate had a dimension grade between 5 and 20 mm, as per ASTM C33, and the cement type used in the mortar was CEM II/B-M.

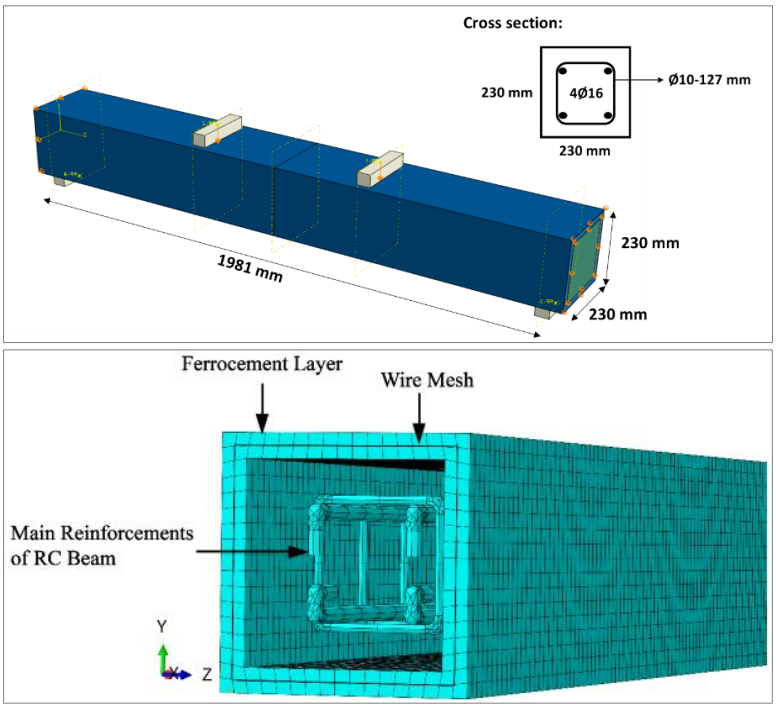

Figure 3. The model of the RC beam retrofitted using a ferrocement layer

2.2. Retrofitting Configurations

To study the effectiveness of ferrocement retrofitting, several models with different retrofitting configurations, as described in Table 1, were considered. The first model CW-1 was the original CM described in the reference model. In the model with ferrocement retrofitting, the applied wire mesh had a yield strength (f_y) of 600 MPa, a diameter of 8 mm, and 100×100 mm of opening. The overlay mortar has a compressive strength (f_m) of 40 MPa and a thickness of 25 mm.

Table 1. Configuration of the models considered in the numerical analyses

No.	Model	Retrofitting description	Layer	Wire mesh orientation	ρ_{wm} (%)	ρ_{mo} (%)
1	CW-1	Without retrofitting	0	-	-	-
2	SS-1-0	Singe sided-1 layer	1	0°	0.48	10.42
3	SS-1-45	Singe sided-1 layer	1	45°	0.48	10.42
4	SS-2-45	Singe sided- 2 layers	2	45°	0.96	20.83
5	DS-1-0	Two-sided - 1 layer	1	0°	0.96	20.83
6	DS-1-45	Two-sided - 1 layer	1	45°	0.96	20.83
7	DS-2-0/0	Two-sided - 2 layers	2	0°	1.92	41.66
8	DS-2-45/45	Two-sided - 2 layers	2	45°	1.92	41.66
9	DS-2-0/45	Two-sided - 2 layers	2	0° and 45°	1.92	41.66

SS: single sided, DS: double sided

SS: single sided, DS: two sided

Models SS-1-0 and SS-1-45 were retrofitted CM models with a single-layer ferrocement reinforcement applied on one side of the wall, as shown in Figure 4-a and b, where the wire mesh orientations are 0° and 45°, respectively. Model SS-2-45 was retrofitted using double-layer ferrocement with a 45° wire mesh orientation and applied on the single side of the wall, as shown in Figure 4-d.

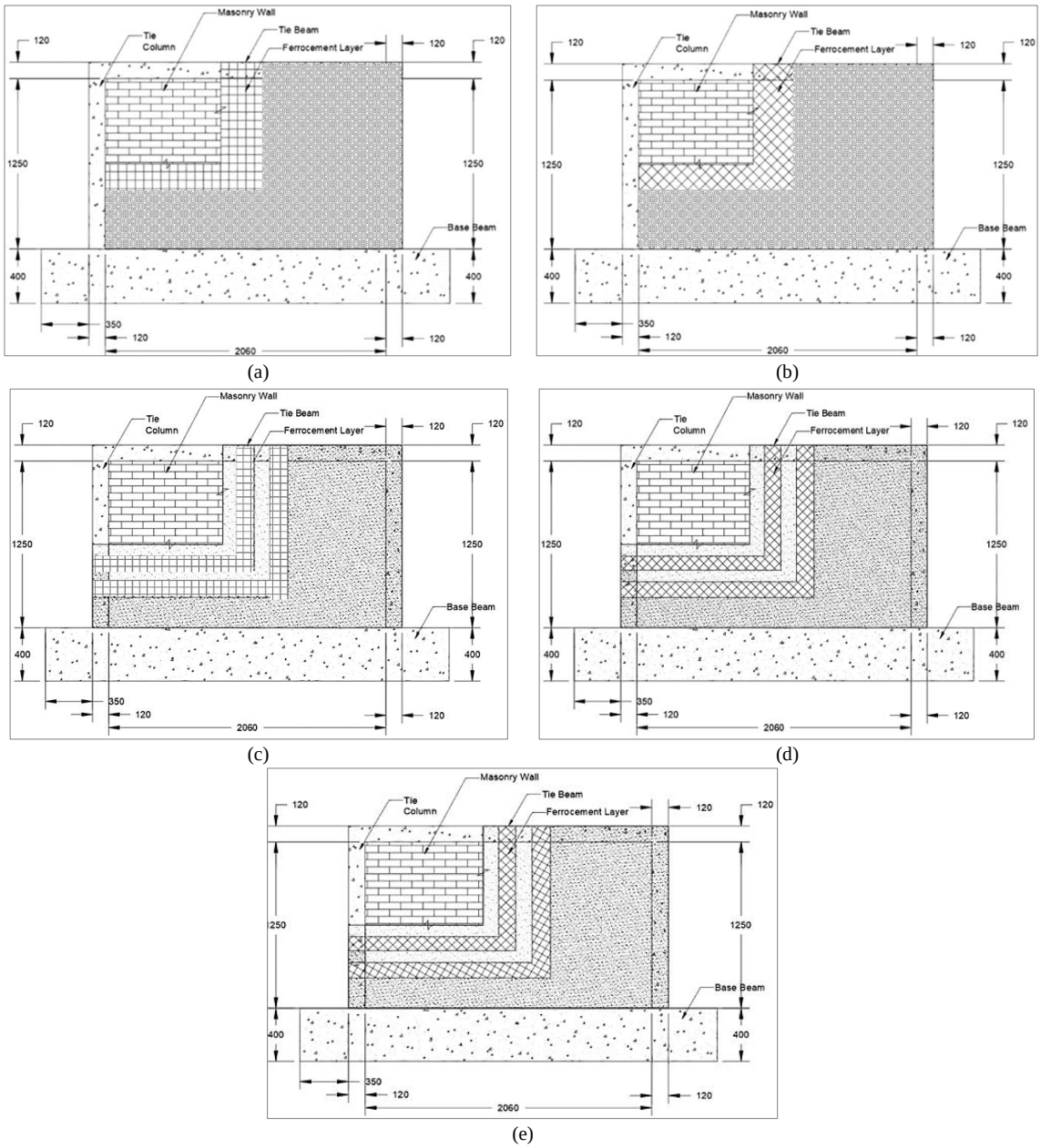

Figure 4. Side-view sketches of the retrofitted models: (a) SS-1-0 and DS-1-0, (b) SS-1-45 and DS-1-45, (c) DS-2-0/0, (d) SS-2-45 and DS-2-45/45, and (e) DS-2-0/45

DS-1-0 and DS-1-45 were CM models with one-layer ferrocement reinforcement applied on both sides of the wall, as shown in Figure 4-a and 4-b, where the wire mesh orientations are 0° and 45°, respectively. Models DS-2-0/0 and DS-2-45/45 were retrofitted on both sides using double-layer ferrocement where the orientations of the wire mesh were 0° and 45°, respectively. Whereas in model DS-2-0/45, the CM model was retrofitted on both sides using a double layer of ferrocement with combined wire mesh orientations of 0° and all 45°, as shown in Figure 4-e.

These nine configurations were considered to evaluate the effects of the volume of the ferrocement layer and the wire mesh orientation. Table 1 shows the volume of the reinforcing elements in Table 1 in terms of the volumetric ratio of the wire mesh to the masonry (ρ_{wm}) and the ratio of the mortar overlay to the masonry (ρ_{mo}). The value of ρ_{wm} ranged from 0.48% to 1.92%, while the value of ρ_{mo} varies from 10.42% to 41.66%.

2.3. Material Model

In general, the numerical modeling of masonry structures can be performed through different approaches: detailed microscale modeling, simplified microscale modeling, and macroscale modeling, as shown in Figure 5. In the detailed micro-model, the masonry unit, mortar, and interfaces between them were separately modeled using specific properties [29–32], as shown in Figure 5-a. Generally, it is realized using continuum elements combined with discontinued elements or contact interfaces. This strategy may result in a more accurate model but a higher computational cost.

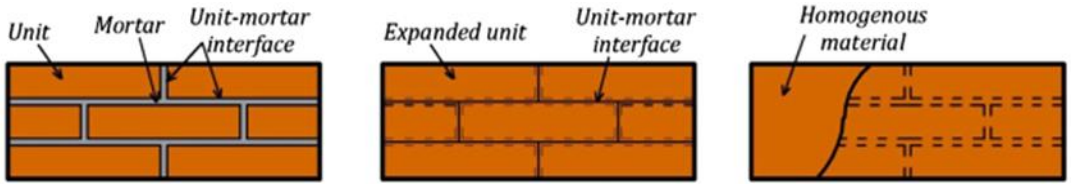

Figure 5. Three alternatives to masonry numerical models: (a) the detailed model, (b) the simplified micro model, and (c) the homogenized model

To compensate for the drawback of detailed micro-modeling, simplified micro-modeling has been proposed in numerous studies [33–36]. In this method, the brick unit and mortar element were modeled as a combined unit element, which is usually called an expanded element; see Figure 5-b. The element was expanded in size by as much as half the mortar thickness. In the interface between the expanded elements, a zero-thickness interface was applied to mimic the elastic-plastic and damage behavior in tension, shear, and compression. This method can reduce computational costs and maintain sufficient accuracy compared to detailed micromodels.

The third model is called the macro model, which employs a continuum model for the entire masonry panel [37-41], as shown in Figure 5-c. The continuum model was modeled as a homogeneous material using the predefined nonlinear properties of the masonry panel. The homogeneous materials are assumed to have a softening anisotropic elastic-plastic behavior. This method is acceptable and efficient for practical purposes of observing the global behavior of masonry structures with relatively low computational costs.

In the present study, using the Abaqus explicit solver, the masonry panel was modeled using an expanded material unit based on the simplified micro model, as described in Figure 5-b. A concrete damage plasticity (CDP) model was adopted to generate the nonlinearity of the expanded masonry units. The CDP model considers both the cracking behavior due to tension and the crushing behavior due to compression. Figure 6 illustrates the material model, which includes the strain softening under tensile stress and strain hardening under compressive stress, combined with the damage index (dt), which generates the evolution of the modulus elasticity (E) during a loading-unloading cycle. The CDP model was also adopted for the concrete and mortar materials in this study.

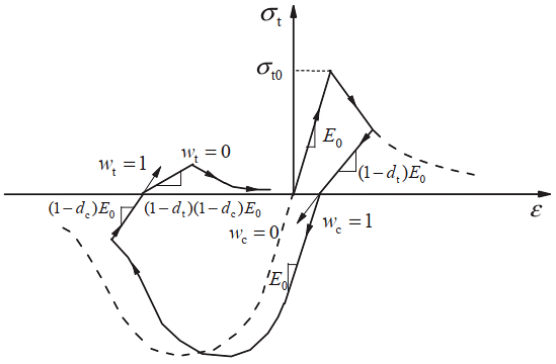

Figure 6. Adopted relationship between the uniaxial stress-strain in compression and tension in a concrete damage plasticity model

The modulus elasticity and Poisson ratio of the expanded brick unit were set to 7845 MPa and 0.2, respectively. To simulate the crushing of the expanded masonry unit under compression, the uniaxial stress-strain as shown in Figure 7-a was adopted. For the nonlinearity of the brick unit in the tension regime, a bilinear softening stress-crack displacement, as shown in Figure 7-b, was adopted. The use of the displacement-stress relationship instead of the strain-stress relationship to model the behavior of masonry under tension has been proposed in several studies [20, 42]. Figure 7-c and d show the evolution of the damage coefficient under compression and tension, respectively.

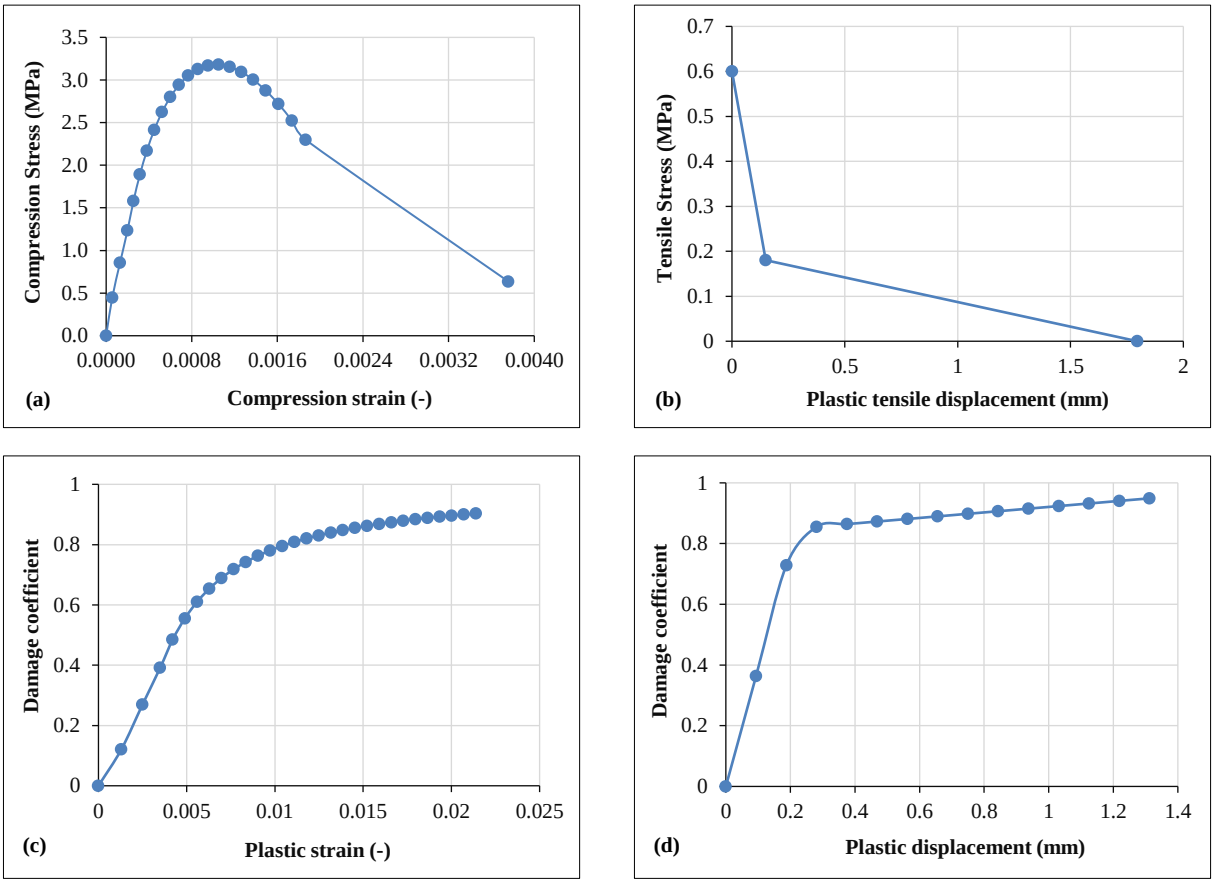

Figure 7. Adopted relationship of (a) uniaxial stress-strain in compression and (b) uniaxial plastic stress-displacement in tension for the expanded unit materials and adopted relationship of damage coefficient-plastic strain or displacement (c) in compression and (d) in tension.

The CDP parameters adopted for the expanded brick unit, concrete, and ferrocement mortar in the present model are described in Table 2, where ε is the eccentricity that controls the potential deviation from the asymptote, K_c is the parameter that defines the deviatoric crushing surface, f_{b0}/f_{c0} is the ratio that defines the yield function, and ψ is the dilatation angle. The interface parameters in the tension and shear regimes between the expanded brick units are given in Table 3. Table 3 Parameters adopted for the interaction between the expanded units.

Table 2. The adopted concrete damage plasticity (CDP) parameters

Materials	ε	Kc	f_{b0}/f_{c0}	ψ
Expanded brick unit	0.1	0.667	1.16	30°
Concrete	0.1	0.667	1.05	36°
Ferrocement mortar	0.1	0.667	1.05	36°

In Table 3, k_n is the normal stiffness, f_t is the tensile strength, G_f^I is the mode-I fracture energy, $k^e_{sx,y}$ is the elastic shear stiffness in the in-plane and out-of-plane directions, respectively, c_0 is the coefficient that can be calculated based on the relationship $c_0 = 0.125\sqrt{f_2}$ as per Chinese masonry structure code (GB 50003-2011) [43], cr is the residual cohesion for the mortar joints that can be calculated based on the relationship c_r=0.06 c0, and G_t^{II} is the mode-II fracture energy.

Table 3. Parameters adopted for the interaction between the expanded units

	Symbol	Bed joints	Head joints
Tension regime	k_n (N/mm^3)	33.11	28.72
	f_t (MPa)	0.12	0.09
	G_f^I (N/mm)	0.022	0.04
Shear regime	$k^e_{sx,y}$ (N/mm^3)	14.40	12.48
	c_0 (MPa)	0.17	0.06
	c_r (MPa)	0.75	0.75
	G_t^{II} (N/mm)	0.22	0.18

As in the masonry model, CDP was also adopted in the concrete-frame model using the parameters listed in Table 2. The modulus elasticity was defined as 22540 MPa, and the Poisson ratio was set to 0.2. The uniaxial stress-stress curves for the concrete under compression and tension are presented in Figures 8-a and 8-b, respectively, which were computed based on the Chinese code GB 50010-2010 [44]. Figure 8-c and d show the evolution of the damage coefficient under compression and tension, respectively. The idealized elastic-plastic stress-strain curve was adopted for the reinforcing bars and confinements, where the yield stress of the steel was set to 400 MPa.

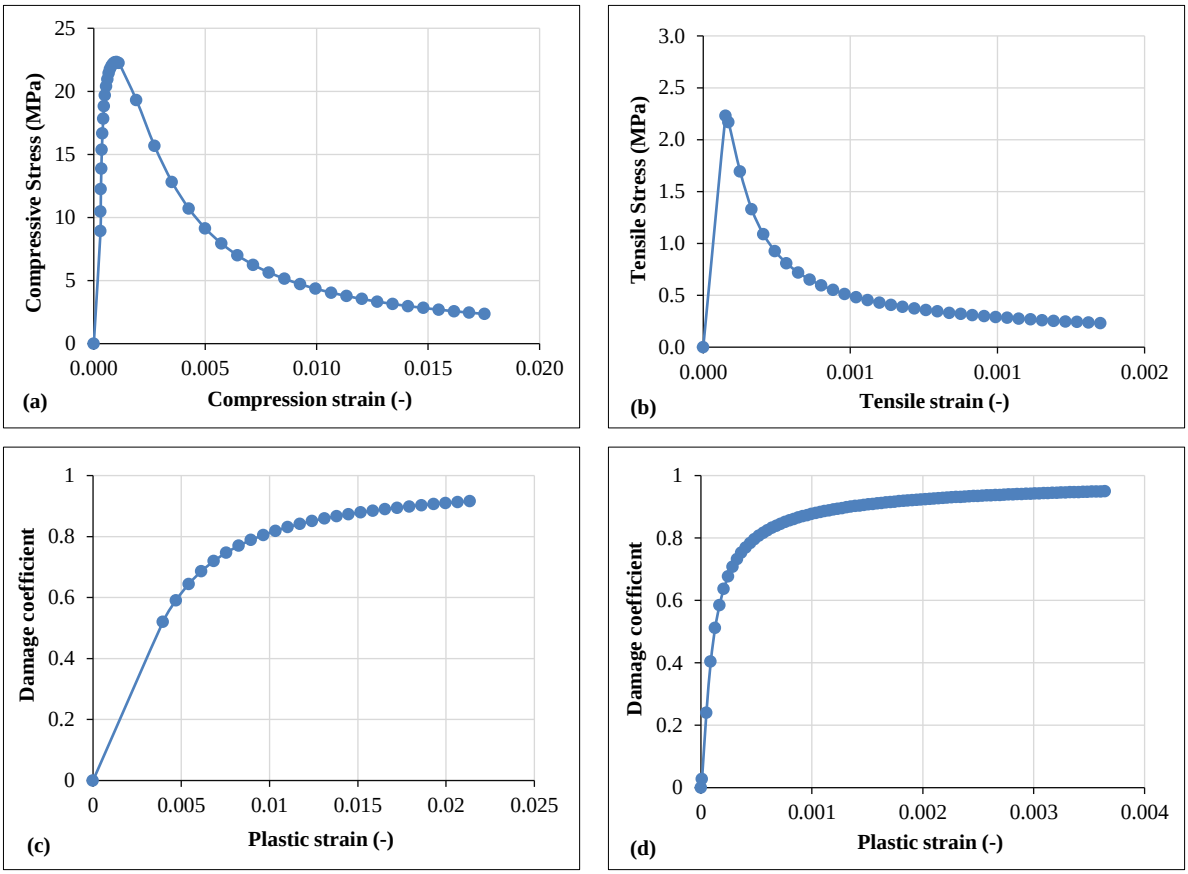

Figure 8. Adopted relationship of (a) uniaxial stress-strain in compression and (b) uniaxial stress-strain in tension for the concrete materials and adopted relationship of damage coefficient-plastic strain (c) in compression and (d) in tension.

The ferrocement retrofitting layer consists of a mortar layer and a wire mesh. In this study, the ferrocement retrofitting experiment reported by Miah et al. [28] was used as the benchmark for model validation. The modulus elasticity of the mortar was defined as 29725 MPa, and the Poisson ratio was set to 0.2. The CDP parameters of the mortar model are listed in Table 2. The uniaxial stress-stress curves of the mortar under compression and tension are presented in Figures 9-a and 9-b, respectively. Figure 9-c and 9-d show the damage evolution during compression and tension, respectively. The idealized elastic-plastic stress-strain of the wire mesh with modulus elasticity and yield strength of 210 GPa and 600 MPa, respectively, was adopted in this study.

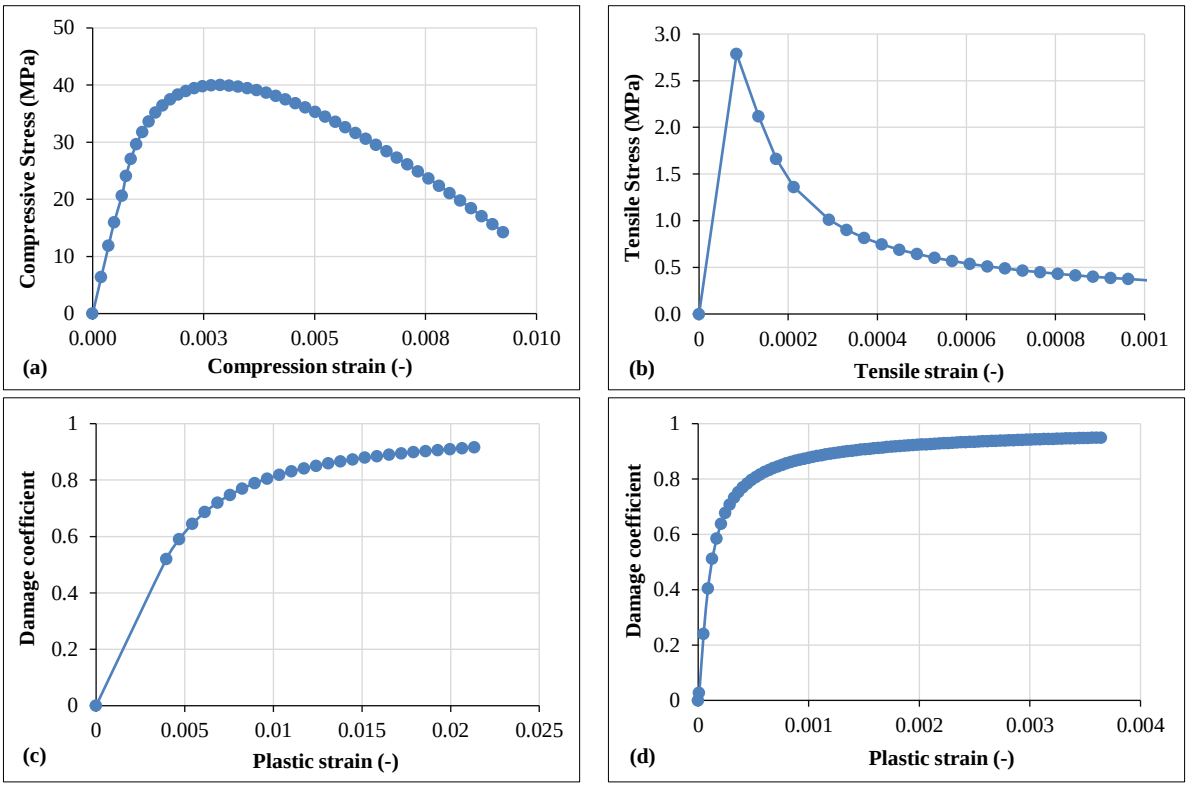

Figure 9. Adopted relationship of (a) uniaxial stress-strain in compression and (b) uniaxial stress-strain in tension for the mortar elements in the ferrocement layer and adopted relationship of damage coefficient-plastic strain (c) in compression and (d) in tension.

2.4. Mesh and Boundary Conditions

In the CM model, the expanded material units of the masonry panel were meshed as reduced integration hexahedral continuum elements (C3D8R) with a size of 30 mm, as shown in Figures 10-a and 10-b. The concrete frames were also modeled using C3D8R elements of various sizes (50–100 mm). Meanwhile, the longitudinal and transversal bar reinforcements and the wire mesh were modeled as linear 2 nodes 3D truss elements (T3D2) with sizes of approximately 50 mm for the longitudinal bars and 25 mm for the transversal bars.

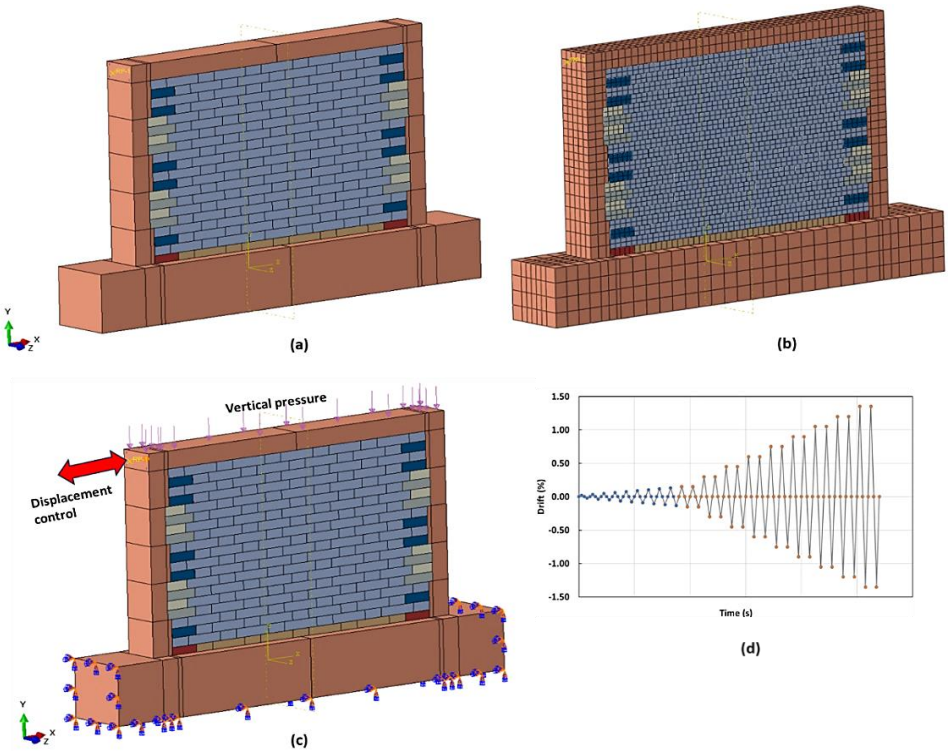

Figure 10. (a) Finite element model of the CM structure, (b) meshing of the model, (c) applied boundary conditions and loads, and (d) displacement control history at the top of the wall

As shown in Figure 11-a, the interaction between the masonry panel and the confining RC frames was considered a tie-constraint. Embedded region-tie interactions were applied for the interaction between the concrete and reinforcement bars, as shown in Figure 11-b, as well as for the interaction between the mortar and wire mesh in the ferrocement layer. Furthermore, the interface between the expanded masonry unit was modeled separately for the bed and head joints, as presented in Figure 11-c, d, and e, where the interaction properties are given in Table 3.

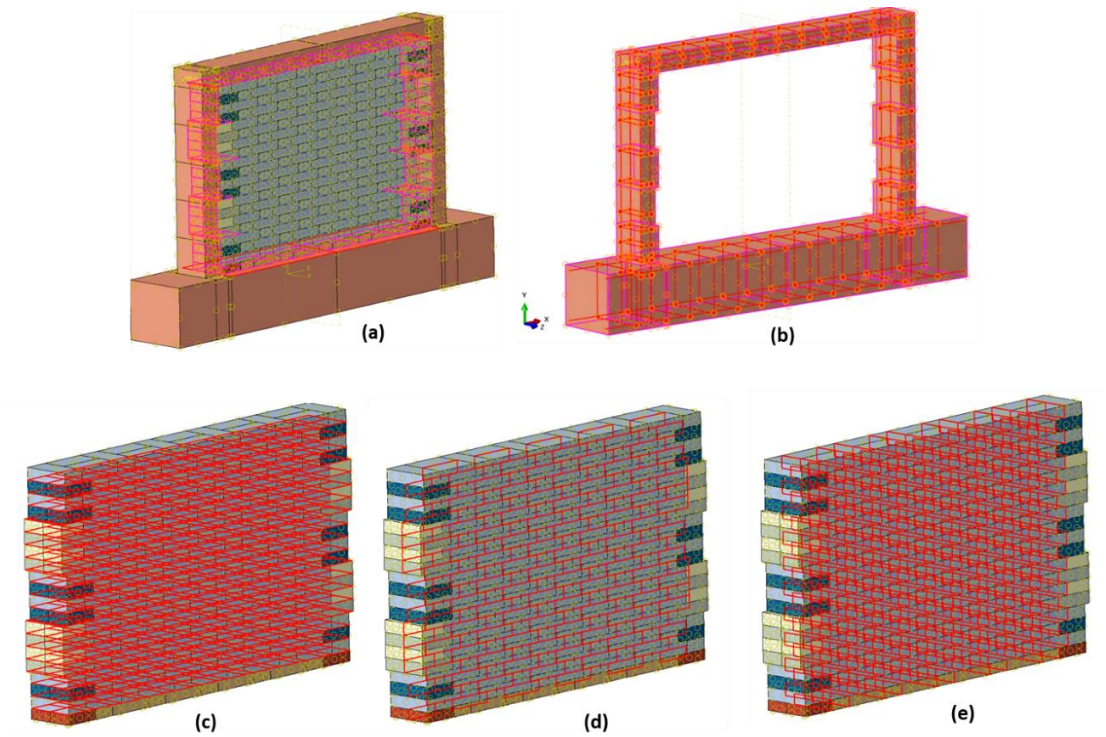

Figure 11. (a) Tie-constraint between the masonry panel and the confining frame, (b) embedded constraint between concrete and reinforcement bars, (c) bed-joint interaction between expanded brick units, and (d, e) head-joint interaction between expanded brick units.

In the present numerical model, the cyclic loading protocol shown in Figures 10-c and 9-d was adopted to capture the hysteretic behavior of the confined masonry specimens. The model was subjected to incremental cyclic lateral loads up to a drift of 1.35%. In addition, to observe the damage evolution on the specimen, all models were also subjected to a static pushover shear test simulation.

For the model with ferrocement retrofitting, as shown in Figure 12-a, the interface between the masonry panel and the ferrocement layers was considered a tie constraint, as well as for the interaction between the mortar and wire mesh in the ferrocement layer. Figure 12-b presents the meshing of the retrofitted model, where the mortar was modeled as C3D8R elements with a size of approximately 75 mm, and the wire mesh was modeled as T3D3 elements with a size of approximately 50 mm.

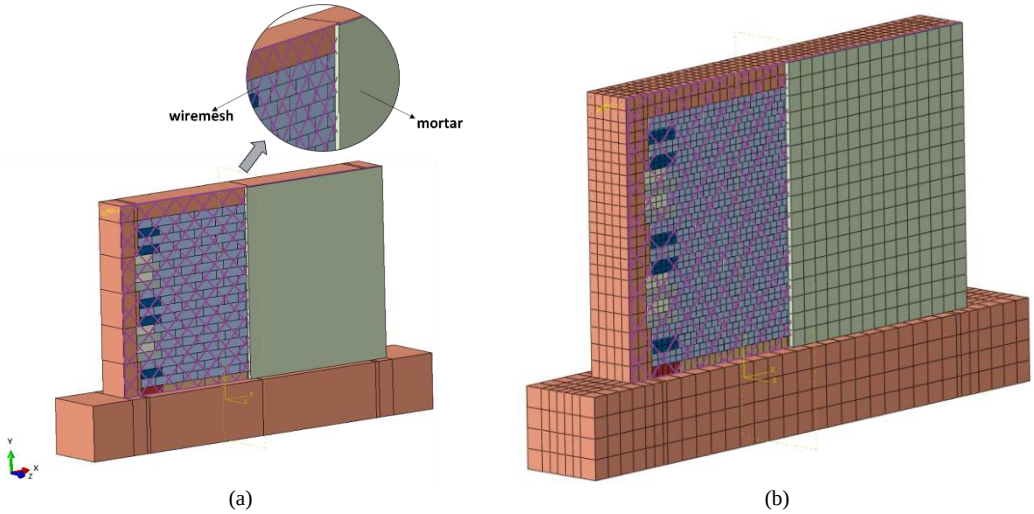

Figure 12. (a) Numerical model of the retrofitted CM structure using the ferrocement layer and (b) meshing of the model

It is worth noting that in reality, the interaction between the retrofitting ferrocement layer and the CM panel is defined by the shear and cohesive strength of the bond. However, to maintain bonding between the ferrocement and the CM panel, a sufficient number of shear connectors in the form of nails or transversal wires can be utilized, as reported in the literature [5, 45].

3. Results and Discussions

3.1. Validation of Numerical Models for Confined Masonry and Ferrocement

The FE analyses were performed using the Abaqus explicit solver. Figure 13-a shows the displacement-force relationship of the original specimen (CW-1) subjected to the cyclic shear test up to 23 mm of top displacement, as obtained from the experimentation in the literature [20]. The backbone curve obtained from the numerical result is in good agreement.

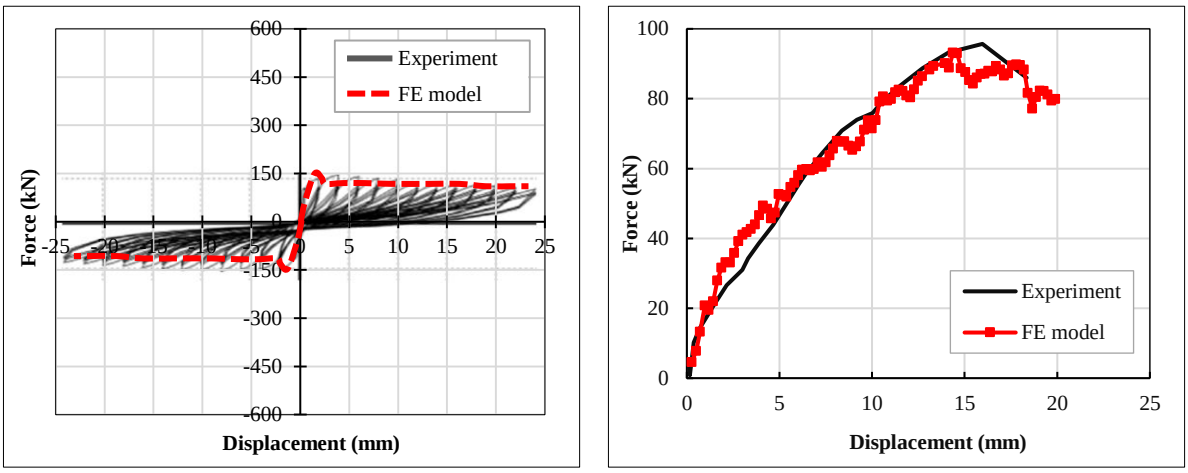

(a) (b)

Figure 13. The force-displacement curves obtained from the experimentation and FE analyses of (a) the original CM structure and (b) the ferrocement-reinforced concrete beam

Figure 13-b presents the comparative results of the displacement-force relationship from the flexural test on a retrofitted RC beam with a ferrocement layer. It was found that the numerical model of the ferrocement-reinforced beam reasonably fits the experimental results reported in the literature [28].

3.2. Result of the Cyclic Shear Test Simulation

A series of cyclic shear test simulations were conducted on the nine CM models up to a maximum drift of 1.35%. The hysteresis force-displacement curves are shown in Figure 14. In general, ferrocement retrofitting resulted in a remarkable increase in the lateral strength and energy dissipation of the CM in all cases.

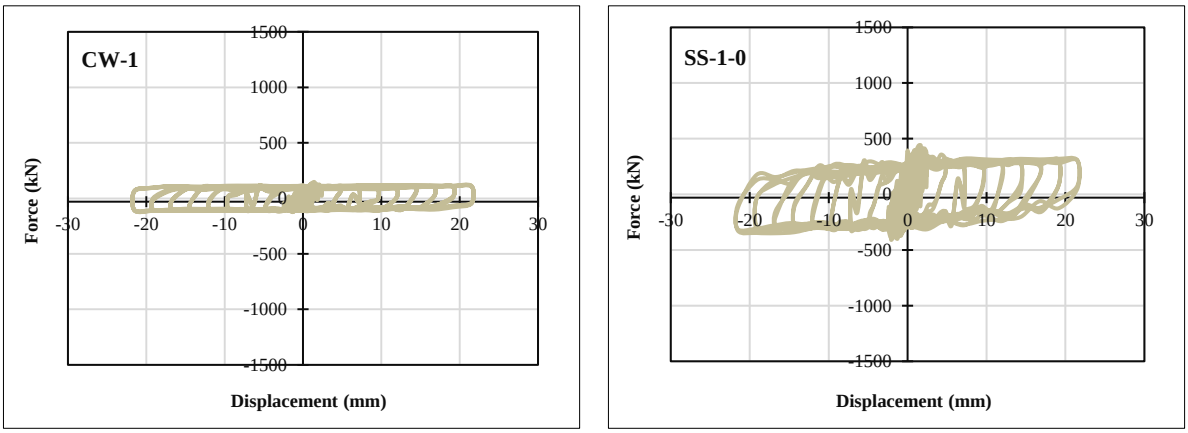

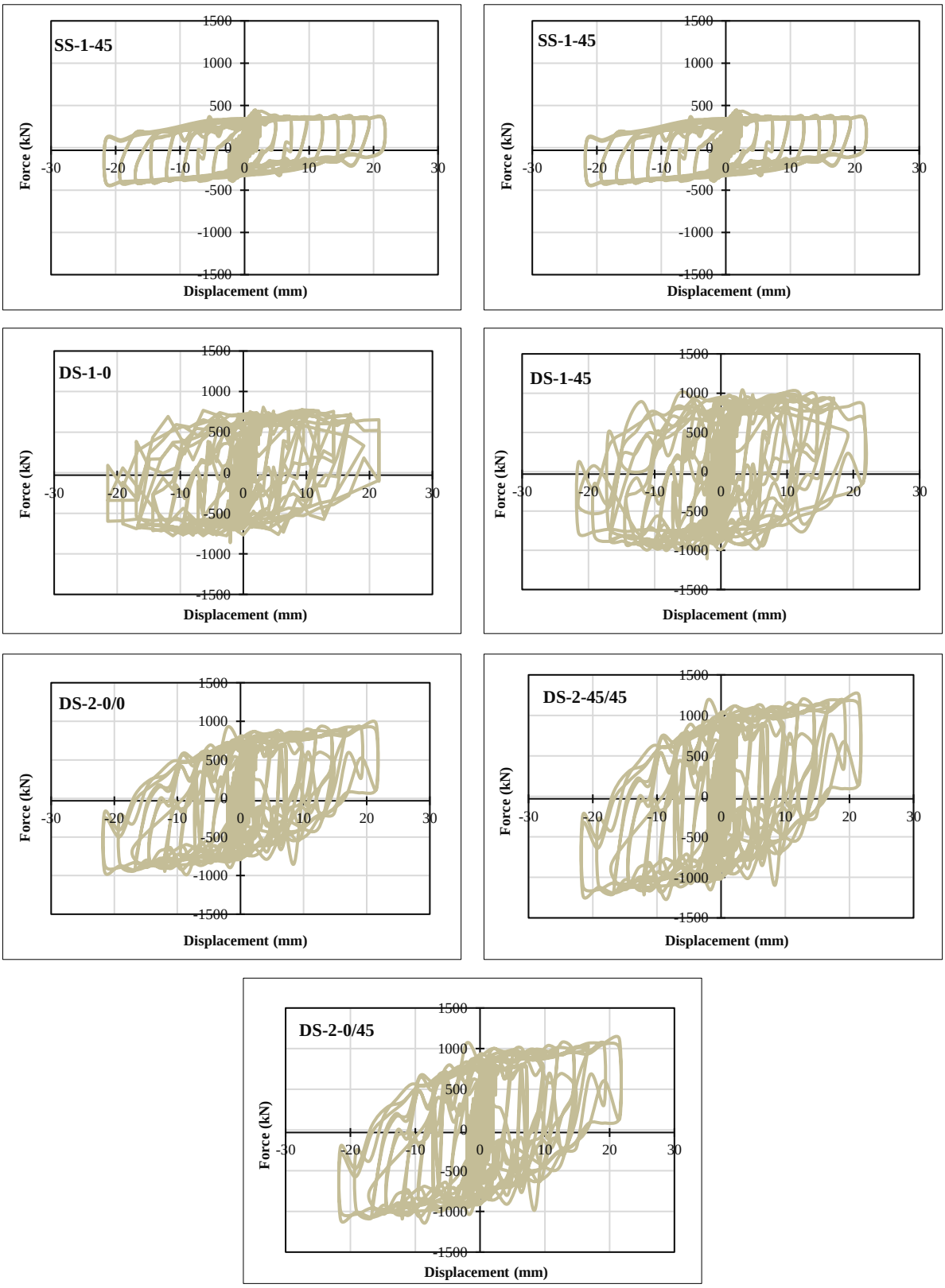

Figure 14. The force-displacement hysteretic curves of the nine models obtained from the cyclic shear test simulations

Based on the obtained hysteretic curves, the backbone curves of each model were generated, as shown in Figure 14, and a summary of the strength and deformability of the models is presented in Table 4. Table 4 lists the maximum lateral load (P_{max}), displacement at Pmax (Δ_{Pmax}), displacement at failure (Δ_u), and ductility factor (μ). The value of Δ_u is the displacement when the lateral load decreases to less than 85% of the maximum lateral load recorded during the simulation. However, up to a drift of 1.35%, not all models presented failure states, for instance, in models SS-2-45, DS-1-0, DS-2-0/0, and DS-2-0/45. Therefore, the ductility coefficient (μ) could not be determined in these three models.

Table 4. Summary of the lateral strength and ductility of the CM models without and with ferrocement reinforcement

Model	P_{max} (kN)	P_{max}/ $P_{max,ori}$	$\Delta_{,Pmax}$ (mm)	Δu (mm)	$\mu = \Delta_u / \Delta_{,Pmax}$	$\mu_,/ \mu_{,ori}$
CW-1	154.90	1.00	1.33	3.26	2.45	1.00
SS-1-0	453.82	2.93	1.45	3.91	2.70	1.10
SS-1-45	460.99	2.98	1.61	7.78	4.83	1.97
SS-2-45	501.96	3.24	1.27	22.00	17.34	7.08
DS-1-0	780.15	5.04	3.64	> 22.0	> 6.04	>2.47
DS-1-45	1023.10	6.60	8.66	21.74	2.51	1.03
DS-2-0/0	910.24	5.88	19.31	> 22.0	N/A	N/A
DS-2-45/45	1194.50	7.71	17.90	>22.0	N/A	N/A
DS-2-0/45	1058.87	6.84	>22.0	> 22.0	N/A	N/A

The ratio of $P_{max}/P_{max,ori}$ indicates the increase factor of the peak lateral load of each model compared to that of the original model without reinforcement (CW-1). As illustrated in Figure 15, the positive effect of applying ferrocement reinforcement was clearly visible. The model with single-side reinforcement, for instance SS-1-0, presented a strength 2.93 times greater than the original model (CW-1).

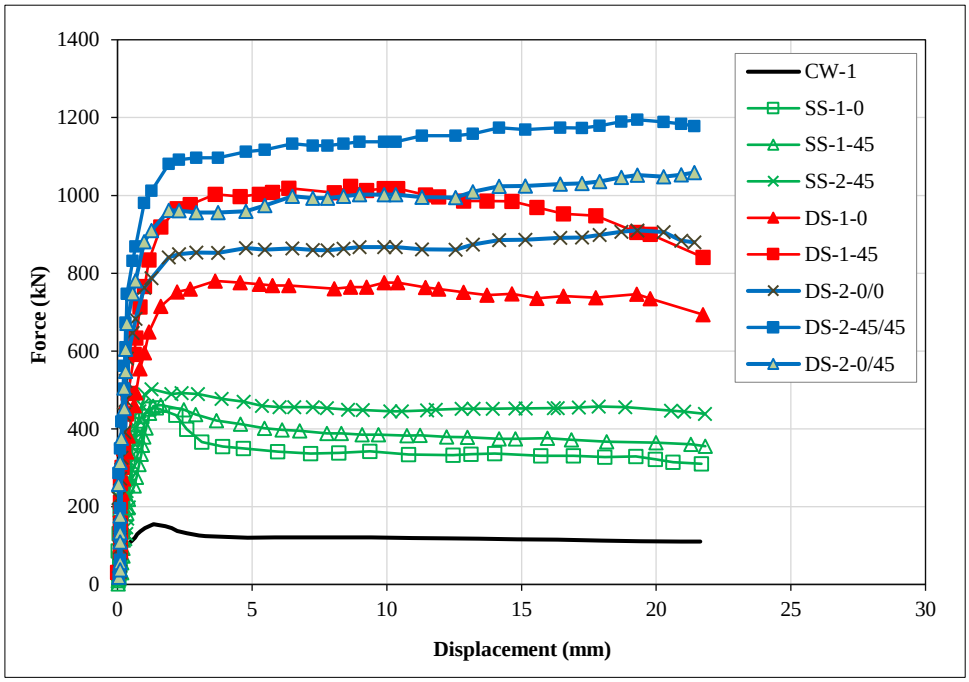

Figure 15. Comparative backbone force-displacement curves of the nine models

Furthermore, in all three models with single-side reinforcement (notated by the initial of SS), the increase factor of Pmax was relatively close. The negligible increase in strength between SS-2-45 and SS-1-45 indicates that in the case of single-side reinforcement, doubling the ferrocement layer on one side does not significantly increase the in-plane shear strength of the panel.

On the other hand, applying ferrocement reinforcement on both sides of the CM panel significantly increased the shear strength, as shown in the comparison between SS-1-0 and DS-1-0, where the increase factor of Pmax increased significantly from 2.93 to 5.04. In addition, when the wire mesh orientation in the two-side reinforcement was set to 45° instead of 0°, the increase factor of the strength increased from 5.04 to 6.6, as shown in the comparison between models DS-1-0 and DS-1-45.

To have an insight into the comparison with experimental tests on ferrocement-retrofitted masonry available in the literature, Table 5 presents the variation of the increase in in-plane shear strength ($P_{max}/ P_{max,ori}$) after retrofitting. ρ_{wm} and ρ_{mo} are the volumetric ratios of the wire mesh and mortar overlay, respectively, to the masonry. f_m is the compressive strength of the mortar overlay, f_y and f_u are the yield and ultimate strength of the wire mesh, respectively. As shown in the table, the range of the increase in strength is wide due to the various wire mesh ratios, overlay mortar ratios, and material specifications.

Table 5. Comparison with other tests in the literature

Ref.	Model	Retrofitting description	Material properties	ρ_{wm} (%)	ρ_{mo} (%)	$P_{max}/P_{max,ori}$
Present study	SS-1-0	Single side	- Mortar overlay f_m=40 MPa - Wire mesh f_y = 600fy=600 MPa	0.480	10.42	2.93
	DS-1-0	Two side		0.960	20.83	5.04
	DS-1-45	Two sides, wire mesh orientation 45°		0.960	20.83	6.60
[12]	TDDS-1	Two sides	- Mortar overlay f_m=27 MPa - Wire mesh f_y= 502 MPa	0.330	83.33	10.24
[13]	RDSS-10	Two sides	- Mortar overlay f_m=2.5 MPa - Wire mesh f_u=873 MPa	0.240	21.74	2.27
[14]	WMCBFS	Two sides	- Mortar overlay, f_m=5 MPa - Wire mesh f_y=450 MPa	0.013	unknown	1.88
	WMOCBFS	Single side		0.007	unknown	1.79
[15]	WD	Two sides	- Mortar overlay, f_m=13 MPa - Wire mesh f_u=697 Mpa	0.094	16.67	1.94
[16]	Stretcher Bond-WM	Two sides	- Mortar overlay, f_m=13 MPa - Wire mesh f_u=697 Mpa	0.034	unknown	2.15

Regarding the effectiveness of doubling the ferrocement layer in the case of two-sided reinforcement, the comparison between DS-1-0 and DS-2-0/0 presented a slight increase in strength, from 5.04 to 5.88, as seen in Table 4, indicating that this configuration did not result in a significant advantage. Moreover, instead of doubling the ferrocement layer, changing the orientation of the single-layer wire mesh to 45° increased the strength from 5.04 to 6.60, as shown in the comparison between DS-1-45 and DS-1-0. The results indicate that the effect of the wire mesh orientation is more significant in defining the lateral strength. Using a wire mesh orientation of 45° instead of 0°, the axial strength of the wires was more effectively exploited during lateral loading. Such a trend was also remarkable for the double layer of ferrocement on both sides of the panel, as shown by the comparison between DS-2-0/0 and DS-2-45/45. On the other hand, combining the wire mesh orientation in the model with a double layer of ferrocement, as shown in model DS-2-0/45, did not have a beneficial effect.

Figure 16 presents a comparison of the increase in ductility when compared to the original specimen (μ/μ,ori). The ductility factor in the three last models could not be computed because their ultimate conditions could not be reached during the numerical analyses. Thus, only six charts in Figure 16 are presented. The greatest increase in ductility was observed for SS-2-45, followed by DS-1-0 and SS-1-45. It is worth noting that doubling the reinforcement layer dramatically enhances the ductility, as shown in the comparison between SS-2-45 and SS-1-45. On the other hand, an increase in ductility was not observed when a single ferrocement layer was applied on both sides of the wall, as presented by the comparison between models SS-1-45 and DS-1-45. However, the latter presented a significant increase in strength, as shown in Figure 17, which should also be a major concern in the selection of strengthening methods for low-rise housing.

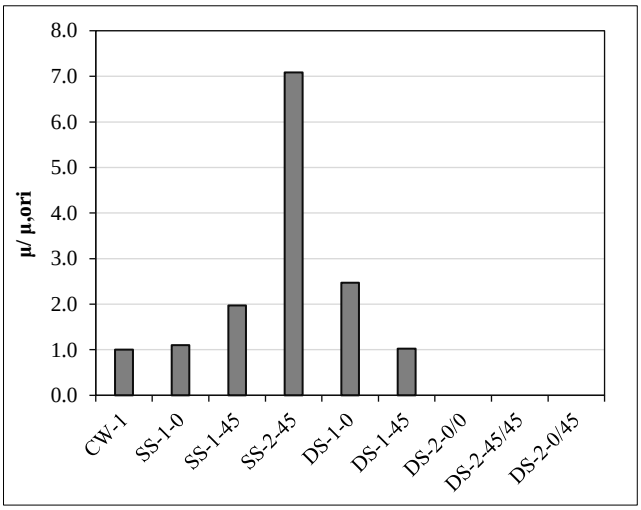

Figure 16. Comparison of the increase in ductility

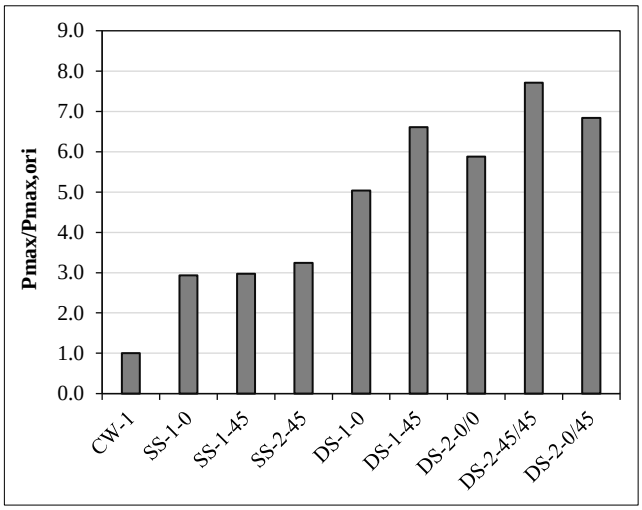

Figure 17. Comparison of the increase in strength

Based on the hysteretic curves obtained from the cyclic shear loading, as shown in Figure 14, the energy dissipation of the models at different drifts was computed, as shown in Table 6 and Figure 18. It was found that, in general, the change in energy dissipation was linearly proportional to the increase in strength, as presented in Figure 17, in which the greatest increase in energy dissipation was observed for model DS-2-45/45. In most models, the energy dissipation decreased slightly with increasing drift ratio. The greatest increase in ductility was observed for SS-2-45, followed by DS-1-0 and SS-1-45. It is worth noting that doubling the reinforcement layer dramatically enhances the ductility, as shown in the comparison between SS-2-45 and SS-1-45. On the other hand, an increase in ductility was not observed when a single ferrocement layer was applied on both sides of the wall, as presented by the comparison between models SS-1-45 and DS-1-45. However, the latter presented a significant increase in strength, as shown in Figure 17, which should also be a major concern in the selection of strengthening methods for low-rise housing.

Table 6. The energy dissipation of the models at different drifts

Model	Wd (kNm)			Wd / Wd,ori		
	Δ=0.15%	Δ=0.60%	Δ=1.35%	Δ=0.15%	Δ=0.60%	Δ=1.35%
CW-1 (original)	0.85	3.95	9.39	1.00	1.00	1.00
SS-1-0	2.76	10.28	22.73	3.24	2.60	2.42
SS-1-45	2.65	11.69	25.95	3.11	2.96	2.76
SS-2-45	3.34	13.89	31.26	3.92	3.52	3.33
DS-1-0	5.22	24.14	52.65	6.12	6.11	5.61
DS-1-45	6.69	30.94	67.50	7.84	7.83	7.19
DS-2-0/0	5.87	26.06	54.81	6.89	6.60	5.84
DS-2-45/45	7.53	33.42	70.27	8.83	8.46	7.49
DS-2-0/45	6.70	29.74	62.54	7.86	7.53	6.66

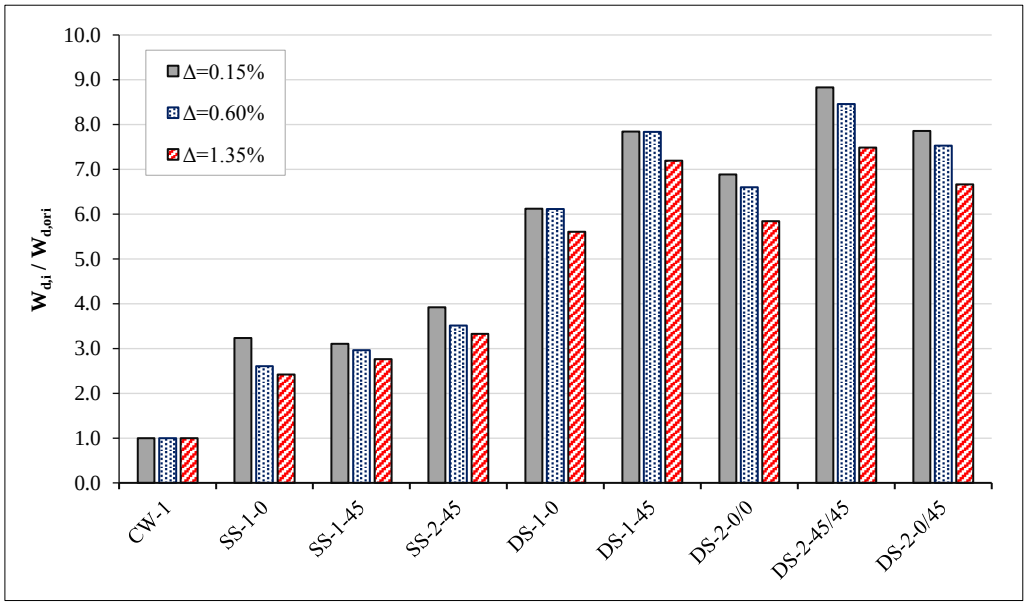

Figure 18. Comparison of the increase in energy dissipation at different drift magnitudes

Based on the hysteretic curves obtained from the cyclic shear loading, as shown in Figure 14, the energy dissipation of the models at different drifts were computed, as shown in Table 6 and Figure 18. It was found that, in general, the change in energy dissipation was linearly proportional to the increase in strength, as presented in Figure 17, in which the greatest increase in energy dissipation was observed for model DS-2-45/45. In most models, the energy dissipation decreased slightly with increasing drift ratio.

3.3. Damage Propagation in Pushover Shear Test Simulations

To observe damage propagation in models undergoing lateral loads, a series of pushover analyses were conducted. Figures 19 to 26 show the comparison of the damage patterns of each model at a displacement of 8 mm, which corresponds to a drift of 0.64%. In the original model CW-1, the damage was mainly characterized by the crack or detachment of the mortar bonds in a diagonal pattern.

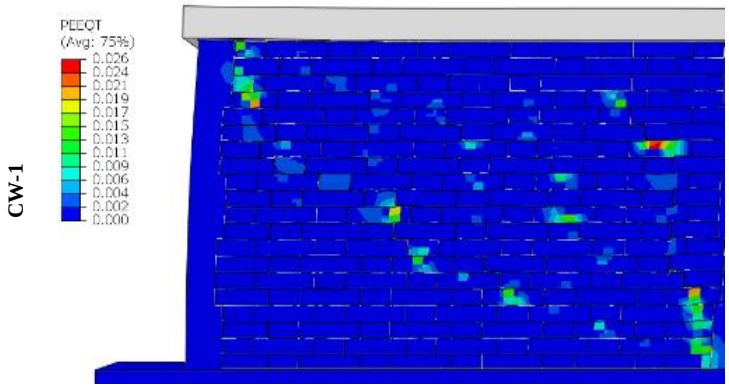

Figure 19. Damage pattern of model CW-1 at drift of 0.64%

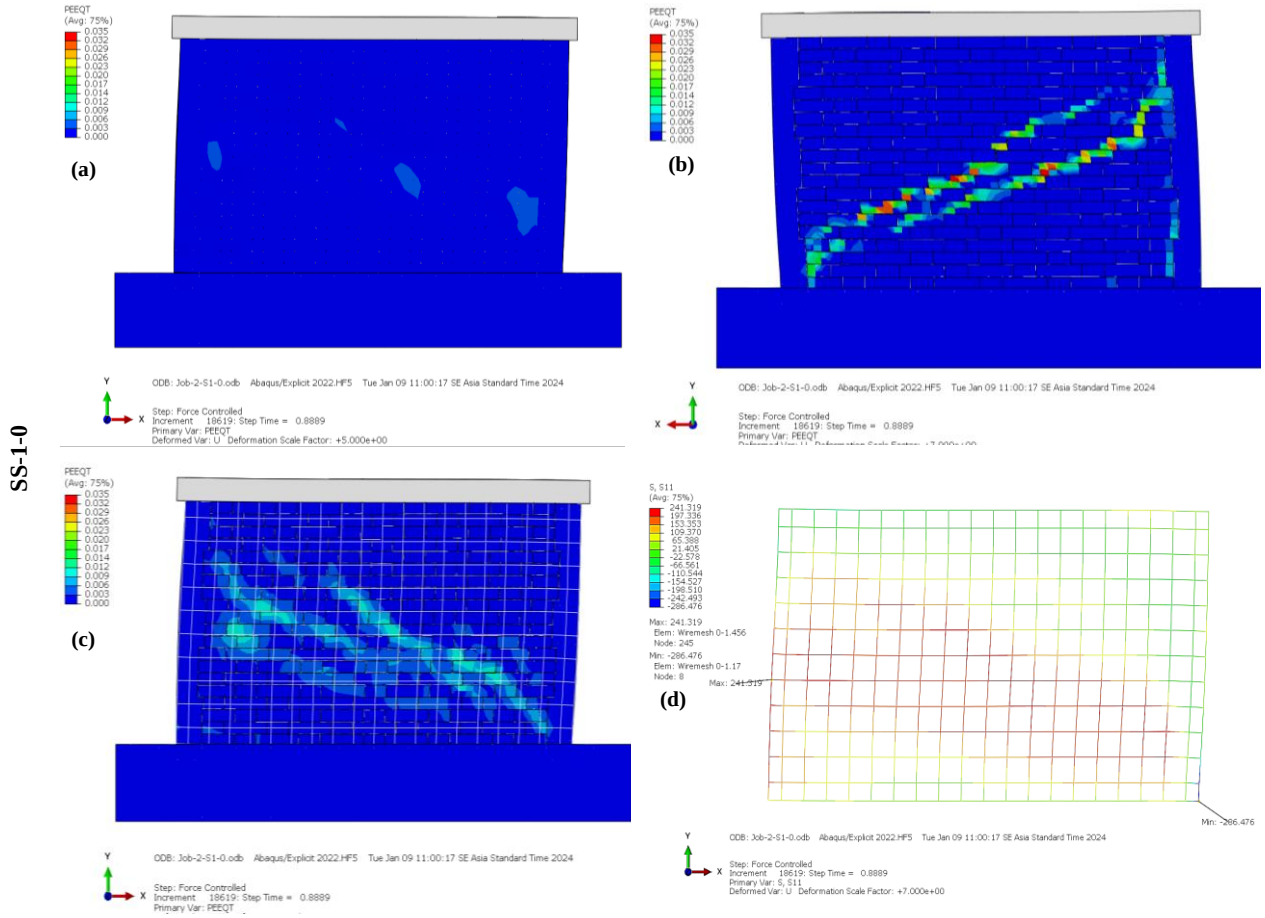

Figure 20. Damage patterns of model SS-1-0 at a drift of 0.64%: (a) retrofitted side, (b) un-retrofitted side, (c) retrofitted side when mortar was hidden, (d) stress on the wire mesh

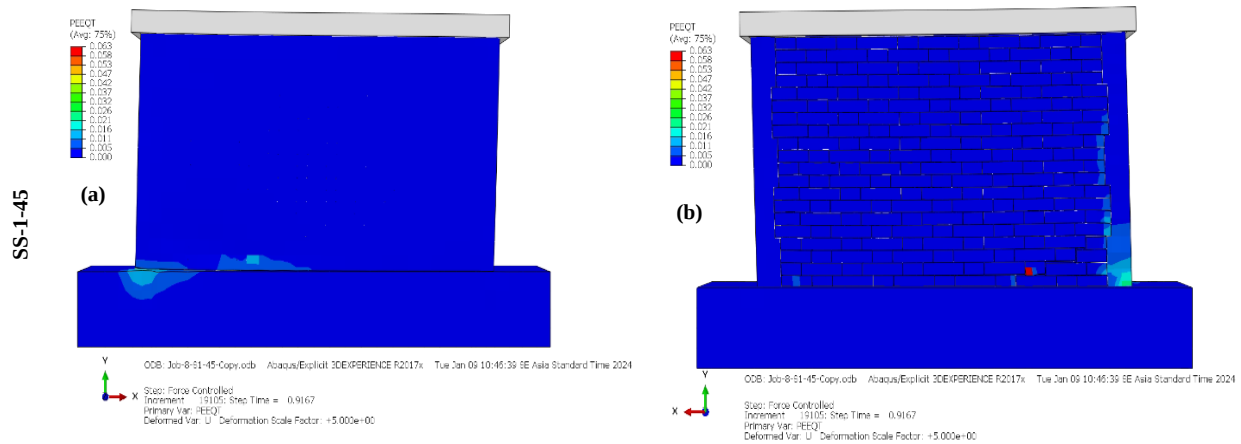

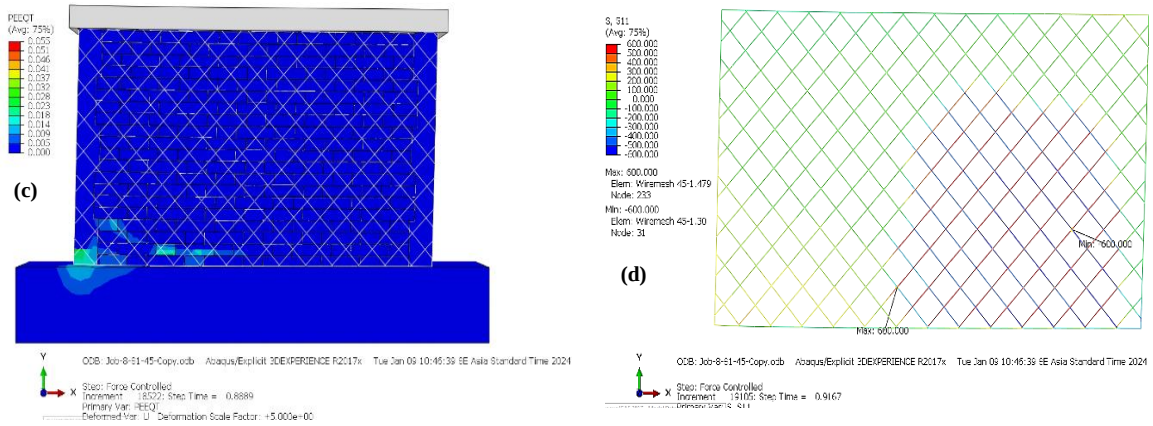

Figure 21. The damage pattern of model SS-1-45 at a drift of 0.64%.: (a) retrofitted side, (b)un-retrofitted side, (c) retrofitted side when the mortar was hidden, (d) stress on the wire mesh.

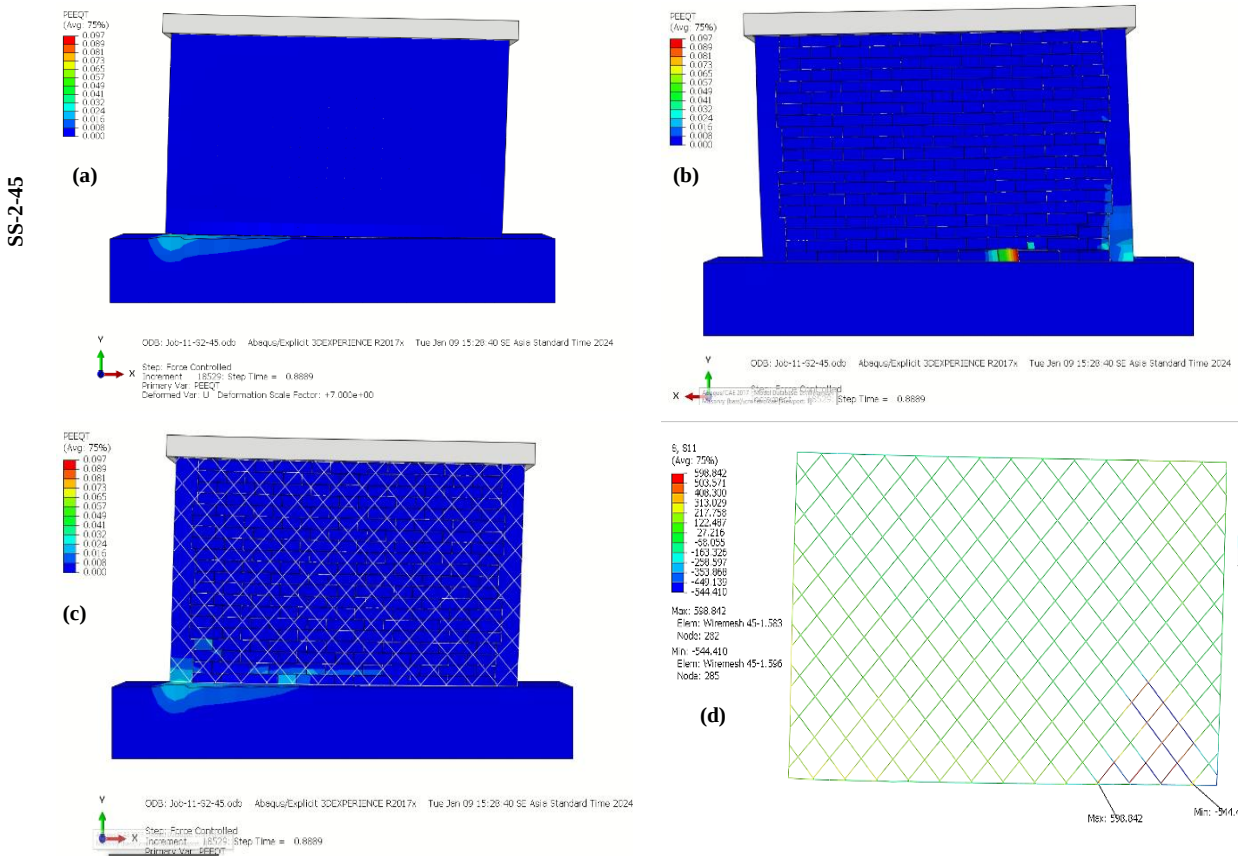

Figure 22. Damage pattern of model SS-2-45 at a drift of 0.6%: (a) retrofitted side, (b)un-retrofitted side, (c) retrofitted side when mortar was hidden, (d) stress on the wire mesh.

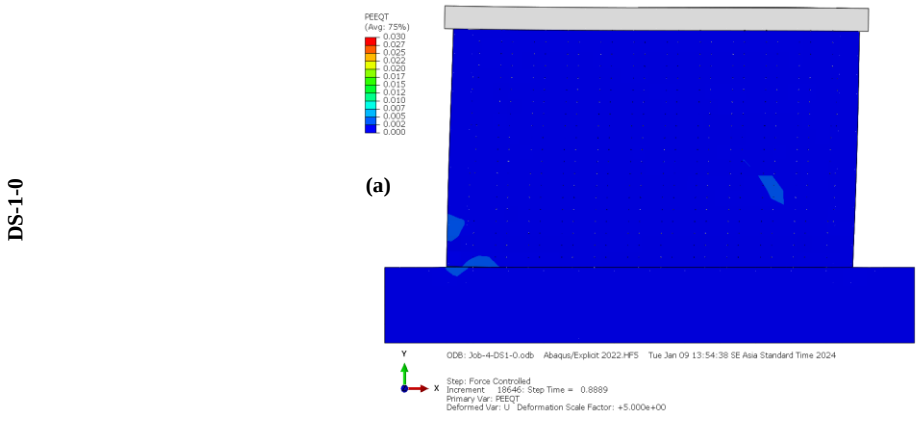

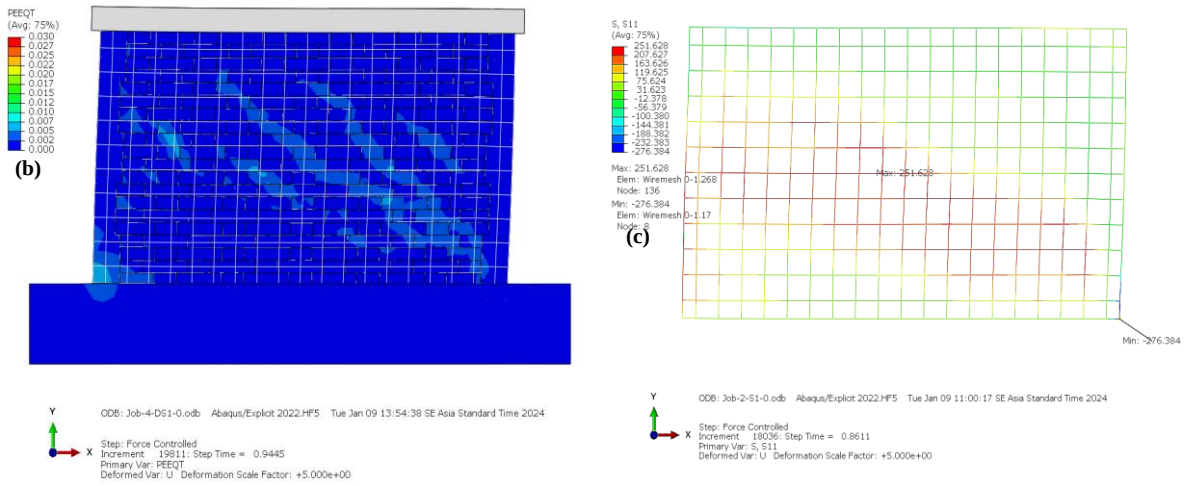

Figure 23. Damage pattern of model DS-1-0 at a drift of 0.64%: (a) retrofitted side, (b) retrofitted side when the mortar was hidden, (c) stress on the wire mesh

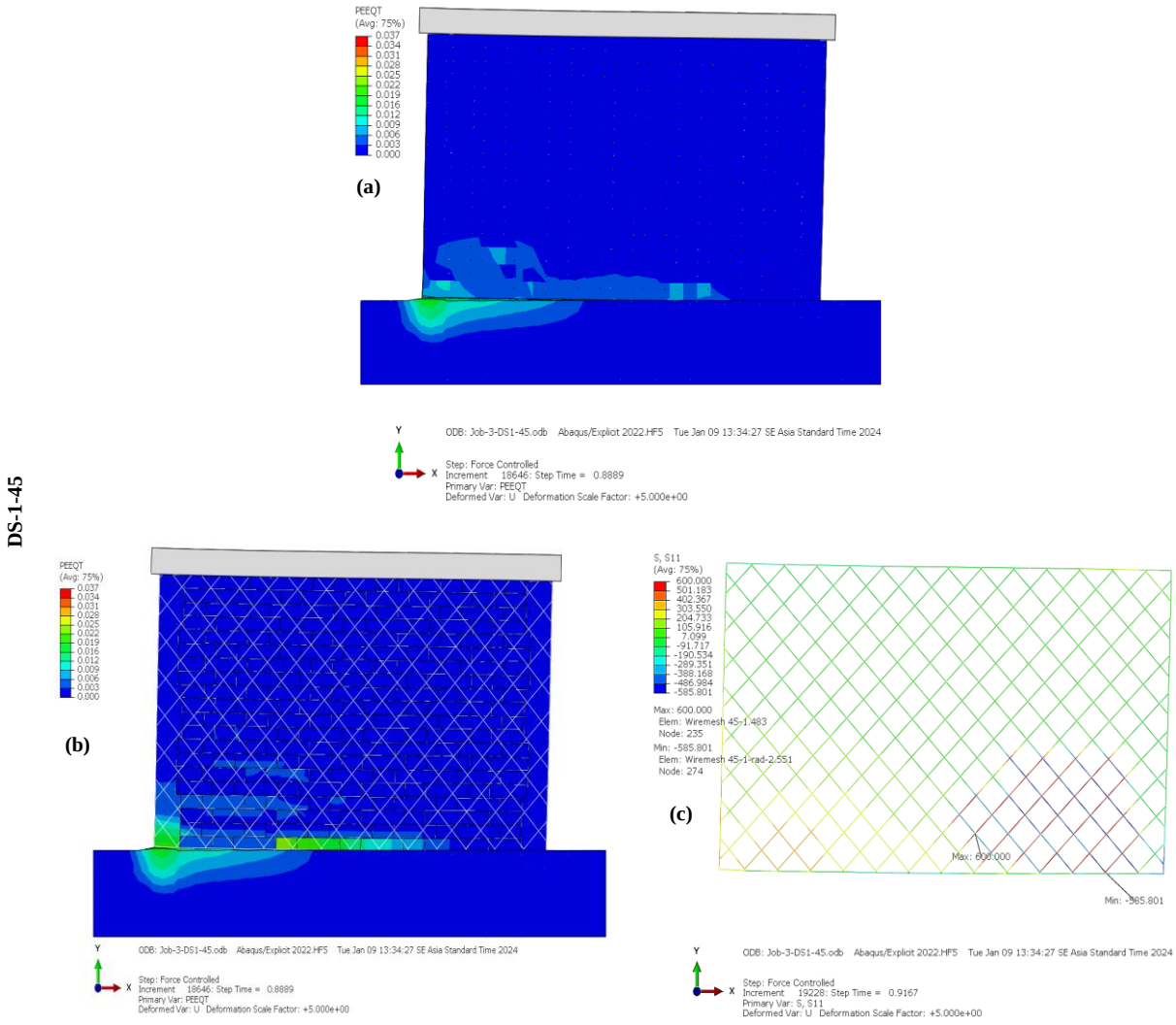

Figure 24. Damage pattern of model DS-1-45 at a drift of 0.64%: (a) retrofitted side, (b) retrofitted side when mortar was hidden, (c) stress on the wire mesh

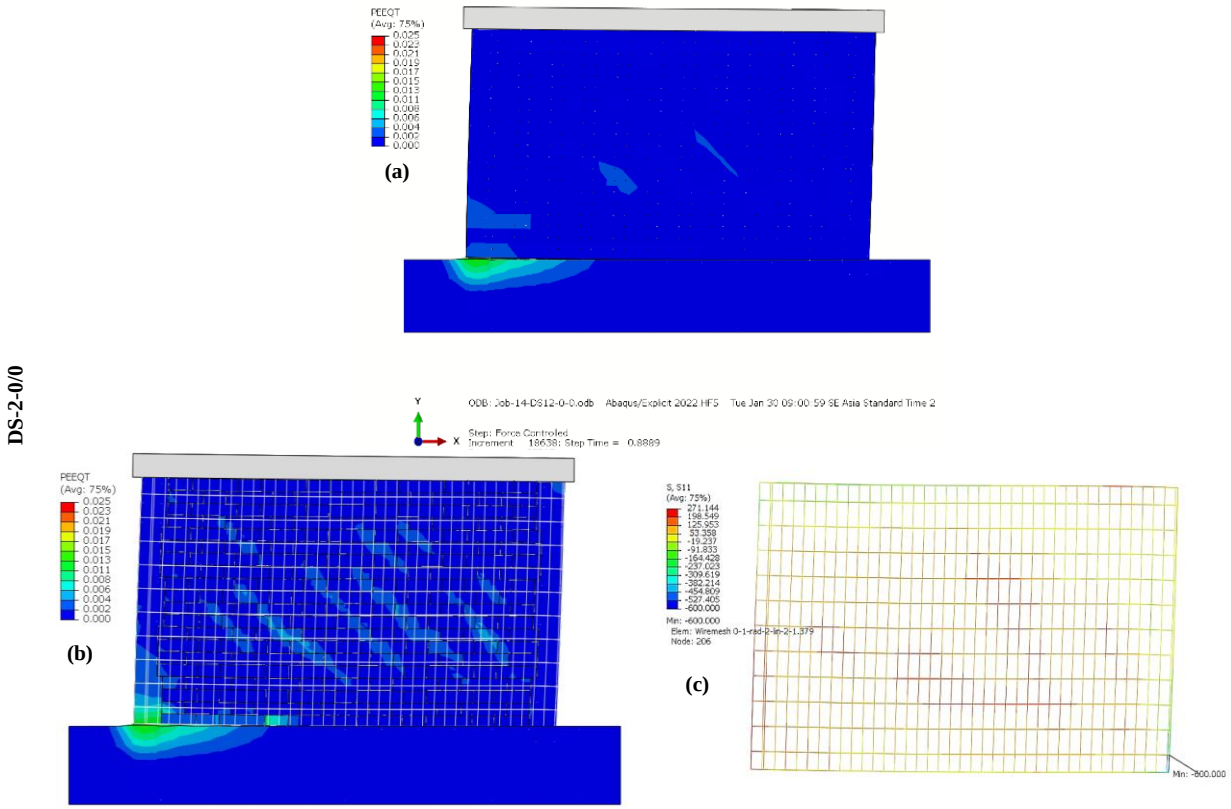

Figure 25. Damage pattern of model DS-2-0/0 at a drift of 0.64%: (a) retrofitted side, (b) retrofitted side when mortar was hidden, (c) stress on the wire mesh

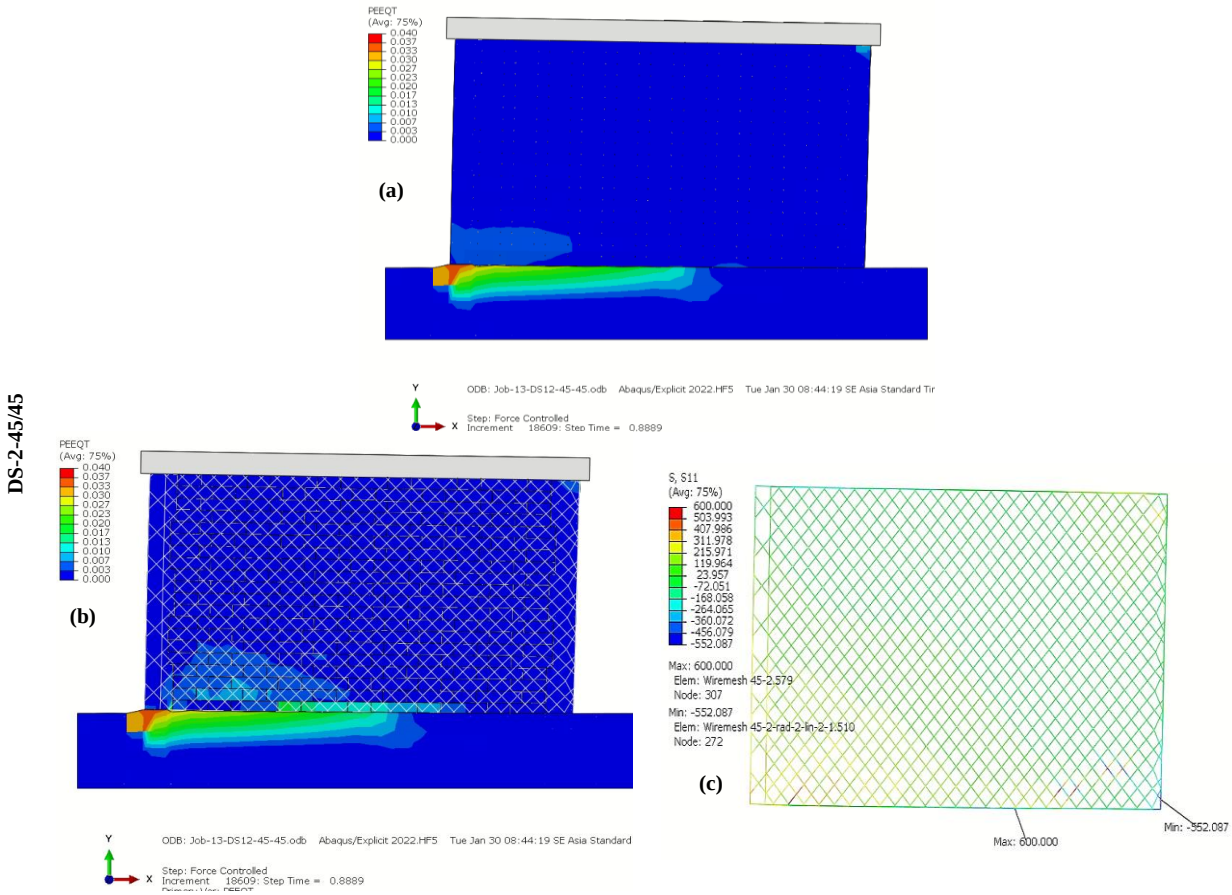

Figure 26. Damage pattern of model DS-2-45/45 at a drift of 0.64%: (a) retrofitted side, (b) retrofitted side when mortar was hidden, (c) stress on the wire mesh

In model SS-1-0, which is not symmetric, the damage patterns of both wall sides were presented, as well as the damage pattern on the masonry when the overlaying mortar layer was hidden. On the retrofitted side, significantly fewer plastic strains were observed than on the unreinforced side. The reinforcing ferrocement layer resulted in a more distributed stress concentration; therefore, the peak magnitude of the plastic strain on the masonry panel was smaller than that on the nonretrofitted side.

In model SS-1-45, where the orientation of the wire mesh was set to 45°, the plastic strain was concentrated at the bottom corner, where rocking failure was dominant. The masonry panel itself was more protected than model SS-1-0. As shown in the induced stress on the wire mesh, the wire in model SS-1-45 experienced much greater stress than that in model SS-1-0. Applying a wire mesh with an orientation of 45° would exploit more of the wire strength, resulting in a more reinforcing effect. However, up to a drift of 0.45%, the wire stress in model SS-1-45 exceeded the yield stress.

When the ferrocement layer was doubled on the single side of the wall, as presented in model SS-2-45, almost the same damage pattern was observed. However, due to the greater volume of reinforcing wire mesh, the number of wires that experienced plastic conditions was much lower, resulting in more ductile failure mechanisms.

In models DS-1-0 and DS-1-45, as seen in Figures 23 and 24, when single-layer ferrocement retrofitting was applied on both wall sides, the damage patterns were symmetrical. Also, as observed in the previous models, the configuration with 45° of wire mesh orientation presented more protection on the masonry panel, as indicated by the dominant damage on the interface between the masonry panel and the foundation beam. The strength of the wires was also more exploited in model DS-1-45, as indicated by the higher induced stress on the wires.

Comparing models DS-2-0/0 and DS-2-45/45, as shown in Figures 25 and 26, where double-layer retrofitting was applied on both wall sides, model DS-2-45/45 presented much more localized damage on the RC foundation beam at the same drift level, indicating more protection on the masonry panel. Furthermore, in both models, no plastic strain was observed on the wire mesh element due to the larger wire mesh volume.

4. Conclusions

A series of finite element analyses (FEA) were conducted to evaluate the effectiveness of ferrocement retrofitting applied on the confined masonry (CM) panels. The FE models were developed using the expanded-unit elements model, which involves zero-thickness interactions between units to mimic the behavior of mortar bonds during compression, tension, and shear. The effects of the number of ferrocement layers and the orientation of the wire mesh were examined in this study via cyclic shear test simulations. In the retrofitted models, the volumetric ratio of the wire mesh to the masonry (ρ_{wm}) ranged from 0.48% to 1.92%, whereas the ratio of the mortar overlay to the masonry (ρ_{mo}) varied from 10.42% to 41.66%. According to the obtained results, several conclusions can be drawn:

- The simplified micro model adopted in this study can reasonably predict the shear behavior of the confined masonry panel with a realistic damage pattern.
- Model DS-2-45/45, with ρ_{wm}= 1.92% and ρ_{mo} =41.66%, and a wire mesh orientation of 45°, exhibited the largest increase (7.71 times) compared to the original model without retrofitting. However, the DS-1-45 model, with ρ_{wm} =0.96% and ρ_{mo}=20.83%, might result in the most cost-effective configuration with a 6.6-fold increase in the lateral strength but only a single ferrocement layer applied on both sides. The smallest increase in strength was observed for model SS-1-0 (2.93 times), with ρ_{wm}= 0.48% and ρ_{mo} =10.42%.
- It was found that models with a wire mesh orientation of 45° presented a significantly greater increase in strength due to the maximum exploitation of the wire strength against the shear deformation of the wall.
- The application of ferrocement retrofitting can enhance the ductility of CM panels. For instance, model SS-2-45 presented approximately 7 times increase in ductility. However, the model that exhibited the largest increase in ductility could not be determined in this study because the numerical analyses of some models could not reach the ultimate state.
- Based on the energy dissipation, it was found that the change in the energy dissipation was generally proportional to the increase in strength.

This numerical analysis was performed with the assumption that the ferrocement layer was perfectly bonded to the masonry surface, which is difficult to achieve in real practice. However, the use of shear connectors in the form of transversal wires or nails can enhance the bond between the masonry and the ferrocement layers, as reported in several experimental works.

5. Declarations

5.1. Author Contributions

Conceptualization, A.B.H. and W.S.; methodology, A.B.H. and M.R.H.; software, M.R.H. and W.S.; validation, M.R.H, W.S., and N.K.; investigation, A.B.H. and M.R.H.; resources, W.S.; data curation, M.R.H. and N.K.; writing—original draft preparation, A.B.H.; writing—review and editing, N.K. and G.M.; visualization, M.R.H. and N.K.; supervision, G.M.; project administration, W.S.; funding acquisition, W.S. All authors have read and agreed to the published version of the manuscript.

5.2. Data Availability Statement

The data presented in this study are available in the article.

5.3. Funding and Acknowledgements

The authors would like to acknowledge the financial support received from Indonesia Endowment Fund for Education (LPDP) through Higher Education Endowment Fund (DAPT) Program 2023/2024 and from The National Research and Innovation Agency (BRIN) through RIIM program with grant number 1179/PKTS/ITS/2023.

5.4. Conflicts of Interest

The authors declare no conflict of interest.

6. References

[1] Xekalakis, G., Pitilakis, D., Zuccaro, G., & Christou, P. (2023). Parametric Analysis of Horizontal Static and Dynamic Behavior in Different Types of Masonry Structures. Civil Engineering Journal (Iran), 9(10), 2578–2591. doi:10.28991/CEJ-2023-09-10-015.

[2] Debnath, P., Halder, L., & Chandra Dutta, S. (2022). Damage survey and seismic vulnerability assessment of unreinforced masonry structures in low-intensity Ambasa earthquake of northeast India. Structures, 44, 372–388. doi:10.1016/j.istruc.2022.08.005.

[3] Brignola, A., Pampanin, S., & Podestà, S. (2009). Evaluation and control of the in-plane stiffness of timber floors for the performance-based retrofit of URM buildings. Bulletin of the New Zealand Society for Earthquake Engineering, 42(3), 204–221. doi:10.5459/bnzsee.42.3.204-221.

[4] A. Gumilang, S., & Rusli, M. (2021). Seismic performance of earthquake resistant simple residential confined masonry house structure based on permen PUPR No.5 of 2016 specification. IOP Conference Series: Earth and Environmental Science, 708(1), 12085. doi:10.1088/1755-1315/708/1/012085.

[5] Habieb, A. B., Rofiussan, F. A., Irawan, D., Milani, G., Suswanto, B., Widodo, A., & Soegihardjo, H. (2023). Seismic Retrofitting of Indonesian Masonry Using Bamboo Strips: An Experimental Study. Buildings, 13(4), 854. doi:10.3390/buildings13040854.

[6] Fikri, R., Dizhur, D., Walsh, K., & Ingham, J. (2019). Seismic performance of Reinforced Concrete Frame with Masonry Infill buildings in the 2010/2011 Canterbury, New Zealand earthquakes. Bulletin of Earthquake Engineering, 17(2), 737–757. doi:10.1007/s10518-018-0476-8.

[7] Al-Chaar, G., Issa, M., & Sweeney, S. (2002). Behavior of Masonry-Infilled Nonductile Reinforced Concrete Frames. Journal of Structural Engineering, 128(8), 1055–1063. doi:10.1061/(asce)0733-9445(2002)128:8(1055).

[8] Bruneau, M. (1994). State‐of‐the‐Art Report on Seismic Performance of Unreinforced Masonry Buildings. Journal of Structural Engineering, 120(1), 230‒251. doi:10.1061/(asce)0733-9445(1994)120:1(230)

[9] Toranzo-Dianderas, L. A., Restrepo, J. I., Carr, A. J., & Mander, J. B. (2004). Rocking confined masonry walls with hysteretic energy dissipators and shake-table validation. 13th World Conf. on Earthquake Engineering, 1-6 August, 2004, Vancouver, Canada.

[10] Marques, R., & Lourenço, P. B. (2019). Structural behaviour and design rules of confined masonry walls: Review and proposals. Construction and Building Materials, 217, 137–155. doi:10.1016/j.conbuildmat.2019.04.266.

[11] Celano, T., Argiento, L. U., Ceroni, F., & Casapulla, C. (2021). In-plane behaviour of masonry walls: Numerical analysis and design formulations. Materials, 14(19), 5780. doi:10.3390/ma14195780.

[12] Sandoval, O. J., Takeuchi, C., Carrillo, J., & Barahona, B. (2021). Performance of unreinforced masonry panels strengthened with mortar overlays reinforced with welded wire mesh and transverse connectors. Construction and Building Materials, 267, 121054. doi:10.1016/j.conbuildmat.2020.121054.

[13] Shermi, C., & Dubey, R. N. (2018). In-plane behaviour of unreinforced masonry panel strengthened with welded wire mesh and mortar. Construction and Building Materials, 178, 195–203. doi:10.1016/j.conbuildmat.2018.04.081.

[14] Banerjee, S., Nayak, S., & Das, S. (2020). Improving the In-Plane Behavior of Brick Masonry Wallet Using PP Band and Steel Wire Mesh. Journal of Materials in Civil Engineering, 32(6). doi:10.1061/(asce)mt.1943-5533.0003159.

[15] Warjri, T., Marbaniang, D. F., & Marthong, C. (2022). In-plane behaviour of masonry walls embedding with steel welded wire mesh overlay with mortar. Journal of Structural Integrity and Maintenance, 7(3), 177–187. doi:10.1080/24705314.2022.2048241.

[16] Debnath, P., Chandra Dutta, S., & Mandal, P. (2023). Lateral behaviour of masonry walls with different types of brick bonds, aspect ratio and strengthening measures by polypropylene bands and wire mesh. Structures, 49, 623–639. doi:10.1016/j.istruc.2023.01.155.

[17] De Santis, S., Casadei, P., De Canio, G., de Felice, G., Malena, M., Mongelli, M., & Roselli, I. (2016). Seismic performance of masonry walls retrofitted with steel reinforced grout. Earthquake Engineering & Structural Dynamics, 45(2), 229–251. doi:10.1002/eqe.2625.

[18] Xin, R., & Ma, P. (2021). Experimental investigation on the in-plane seismic performance of damaged masonry walls repaired with grout-injected ferrocement overlay. Construction and Building Materials, 282, 122565. doi:10.1016/j.conbuildmat.2021.122565.

[19] Saingam, P., Hlaing, H. H., Suwannatrai, R., Ejaz, A., Hussain, Q., Khan, K., & Joyklad, P. (2023). Enhancing the flexural behavior of brick masonry walls with ferrocement overlays and low-cost anchors. Case Studies in Construction Materials, 19, 2558. doi:10.1016/j.cscm.2023.e02558.

[20] Deng, M., & Yang, S. (2020). Experimental and numerical evaluation of confined masonry walls retrofitted with engineered cementitious composites. Engineering Structures, 207, 110249. doi:10.1016/j.engstruct.2020.110249.

[21] Umair, S. M., Numada, M., Amin, M. N., & Meguro, K. (2015). Fiber reinforced polymer and polypropylene composite retrofitting technique for masonry structures. Polymers, 7(5), 963–984. doi:10.3390/polym7050963.

[22] Jang, H. S., An, J. H., Song, J. H., Son, S. H., Hong, Y. S., & Eun, H. C. (2022). Out-of-Plane Strengthening of Unreinforced Masonry Walls by Glass Fiber-Reinforced Polyurea. Civil Engineering Journal (Iran), 8(1), 145–154. doi:10.28991/CEJ-2022-08-01-011.

[23] Chourasia, A., Singhal, S., & Parashar, J. (2019). Experimental investigation of seismic strengthening technique for confined masonry buildings. Journal of Building Engineering, 25, 100834. doi:10.1016/j.jobe.2019.100834.

[24] Habieb, A. B., Valente, M., & Milani, G. (2019). Hybrid seismic base isolation of a historical masonry church using unbonded fiber reinforced elastomeric isolators and shape memory alloy wires. Engineering Structures, 196, 109281. doi:10.1016/j.engstruct.2019.109281.

[25] Boni, C., & Royer-Carfagni, G. (2023). Transparent hybrid glass-steel bracing to improve the seismic capacity of historic buildings with colonnades. Engineering Structures, 278, 115522. doi:10.1016/j.engstruct.2022.115522.

[26] Li, J., Wu, C., Hao, H., Su, Y., & Li, Z. X. (2017). A study of concrete slabs with steel wire mesh reinforcement under close-in explosive loads. International Journal of Impact Engineering, 110, 242–254. doi:10.1016/j.ijimpeng.2017.01.016.

[27] Garg, A., Sageman-Furnas, A. O., Deng, B., Yue, Y., Grinspun, E., Pauly, M., & Wardetzky, M. (2014). Wire mesh design. ACM Transactions on Graphics, 33(4). doi:10.1145/2601097.2601106.

[28] Miah, M. J., Miah, M. S., Alam, W. B., Lo Monte, F., & Li, Y. (2019). Strengthening of RC beams by ferrocement made with unconventional concrete. Magazine of Civil Engineering, 89(5), 94–105. doi:10.18720/MCE.89.8.

[29] Scacco, J., Milani, G., & Lourenço, P. B. (2021). A micro-modeling approach for the prediction of TRM bond performance on curved masonry substrates. Composite Structures, 256, 113065. doi:10.1016/j.compstruct.2020.113065.

[30] Anas, S. M., Alam, M., & Umair, M. (2022). Behavior and damage assessment of monolithic and non-monolithic braced masonry walls subjected to blast loadings using a detailed micro-modeling approach. International Journal of Masonry Research and Innovation.

[31] Rotunno, T., Fagone, M., Ranocchiai, G., & Grande, E. (2022). Micro-mechanical FE modelling and constitutive parameters calibration of masonry panels strengthened with CFRP sheets. Composite Structures, 285, 115248. doi:10.1016/j.compstruct.2022.115248.

[32] Moradi, N., Yazdani, M., Janbozorgi, F., & Hashemi, S. J. (2024). In-plane seismic performance of historical masonry walls with various brick bond patterns using micro-modeling approach. Asian Journal of Civil Engineering, 25(6), 4863–4876. doi:10.1007/s42107-024-01085-x.

[33] Dhanasekar, M., & Haider, W. (2008). Explicit finite element analysis of lightly reinforced masonry shear walls. Computers and Structures, 86(1–2), 15–26. doi:10.1016/j.compstruc.2007.06.006.

[34] Agnihotri, P., Singhal, V., & Rai, D. C. (2013). Effect of in-plane damage on out-of-plane strength of unreinforced masonry walls. Engineering Structures, 57, 1–11. doi:10.1016/j.engstruct.2013.09.004.

[35] Minaie, E., Moon, F. L., & Hamid, A. A. (2014). Nonlinear finite element modeling of reinforced masonry shear walls for bidirectional loading response. Finite Elements in Analysis and Design, 84, 44–53. doi:10.1016/j.finel.2014.02.001.

[36] Alforno, M., Monaco, A., Venuti, F., & Calderini, C. (2021). Validation of Simplified Micro-models for the Static Analysis of Masonry Arches and Vaults. International Journal of Architectural Heritage, 15(8), 1196–1212. doi:10.1080/15583058.2020.1808911.

[37] Maccarini, H., Vasconcelos, G., Rodrigues, H., Ortega, J., & Lourenço, P. B. (2018). Out-of-plane behavior of stone masonry walls: Experimental and numerical analysis. Construction and Building Materials, 179, 430–452. doi:10.1016/j.conbuildmat.2018.05.216.

[38] Tiberti, S., Acito, M., & Milani, G. (2016). Comprehensive FE numerical insight into Finale Emilia Castle behavior under 2012 Emilia Romagna seismic sequence: Damage causes and seismic vulnerability mitigation hypothesis. Engineering Structures, 117, 397–421. doi:10.1016/j.engstruct.2016.02.048.

[39] Habieb, A. B., Valente, M., & Milani, G. (2019). Base seismic isolation of a historical masonry church using fiber reinforced elastomeric isolators. Soil Dynamics and Earthquake Engineering, 120, 127–145. doi:10.1016/j.soildyn.2019.01.022.

[40] Shehu, R. (2021). Implementation of Pushover Analysis for Seismic Assessment of Masonry Towers: Issues and Practical Recommendations. Buildings, 11(2), 71. doi:10.3390/buildings11020071.

[41] Guo, K., Habieb, A. B., & Milani, G. (2024). Simulation for a Low-Rise Masonry House Using Seismic Isolator with and Without S-shaped Steel Dampers. Recent Advances in Structural Health Monitoring and Engineering Structures. SHM&ES 2023, Lecture Notes in Civil Engineering, 460. Springer, Singapore. doi:10.1007/978-981-97-0399-9_9.

[42] Park, K., Paulino, G. H., & Roesler, J. R. (2008). Determination of the kink point in the bilinear softening model for concrete. Engineering Fracture Mechanics, 75(13), 3806–3818. doi:10.1016/j.engfracmech.2008.02.002.

[43] GB 50003-2011. (2011). Code for Design of Masonry Structures. China Standard Press, Beijing, China.

[44] GB 50010-2010. (2010). Code for Design of Concrete Structures. China Standard Press, Beijing, China.

[45] Boen, T., Imai, H., Ismail, F., Hanazato, T., & Lenny. (2015). Brief report of shaking table test on masonry building strengthened with ferrocement layers. Journal of Disaster Research, 10(3), 551–557. doi:10.20965/jdr.2015.p0551.